International Journal of Solids and Structures 46 (2009) 989–1006

Contents lists available at ScienceDirect

International Journal of Solids and Structures

journal homepage: www.elsevier.com/locate/ijsolstr

Local probabilistic homogenization of two-dimensional model foams accounting for micro structural disorder

Volker Hardenacke, Jörg Hohe *

Fraunhofer Institut für Werkstoffmechanik, Wöhlerstr. 11, 79108 Freiburg, Germany

ARTICLE INFO

Article history:
Received 25 September 2007
Received in revised form 29 January 2008
Available online 21 October 2008

Keywords:
Solid foams
Micro structural disorder
Effective properties
Numerical homogenization
Stochastic methods

ABSTRACT

The objective of the present study is a numerical analysis of disorder effects in solid structural foams caused by their random irregular micro structure. Using a strain energy based concept, the effective material response is computed in a geometrically non-linear homogenization analysis. The probabilistic homogenization is based on the analysis of a large scale statistically representative volume element. The stochastic information about the scatter in the material response on the lowest possible level is generated by a subsequent division of the representative volume element in substructures consisting of a single cell wall intersection and parts of the adjacent cell walls. For each of the substructures, a homogenization analysis is performed. The results for the local effective stress and strain components are evaluated by means of stochastic methods. The approach is illustrated by a number of examplary studies on the uncertainty of the effective material response of two-dimensional model foams with linear and non-linear elastic material behavior on the cell wall level of structural hierarchy.

1. Introduction

Solid structural foams are important materials in modern lightweight construction which are used as core materials for sandwich structures as well as in other applications. The main advantage of structural foams is their low specific weight at reasonable stiffness and strength levels. The classical field for application of lightweight principles is the aerospace industry. Nevertheless, in the recent time, an increasing demand for lightweight structures can be observed in other technological fields, especially in the automotive industry (Ning et al., 2007), railway technology (Kim et al., 2007) or the naval industry (Mouritz et al., 2001) where both, regular honeycomb type cellular structures and micro structurally disordered foams are used. A second important property of solid foams for structural application is their high energy absorption capacity due to their high compressibility. In conjunction with the almost constant stress level during a wide range of compression, this feature makes solid foams a natural choice for all kinds of shock absorbing systems such as crash elements in automotive application or personal protection systems such as safety helmets etc. (Boomsma et al., 2003; Mills et al., 2003).

In the industrial design process, the numerical analysis of structures and components consisting partly or completely of foamed materials is preferrably performed in terms of the macroscopic "effective" properties rather than by detailed models of the given micro structure. The determination of the effective properties can be performed either by experimental measurements or, at least in an assisting manner, by numerical predictions. Theoretical and numerical approaches play an important role for the identification and description of the underlying microscopic deformation and failure mechanisms. Furthermore, theoretical and numerical analyses might reduce the experimental expenses during the design and optimization of materials for specific applications caused by extensive testing.

Since the pioneering studies by Gent and Thomas (1963) as well as by Patel and Finnie (1970) appeared, numerous studies on the effective properties of foams and other low density cellular solids have been published. Most theoretical and numerical studies in this area are based on the analysis of an idealized regular model for the foam micro structure such as the Kelvin's (1887) tetrakaidecahedral foam model used e.g. by Warren and Kraynik (1988) or the cubic foam model proposed by Gibson and Ashby (1982, 1997). Other important regular periodic micro structural models used in the homogenization analysis of solid foams are the pentagonal dodecahedral cell model proposed by Christensen (1987) which, in contrast to the models mentioned previously, has the advantage to yield isotropic results or the more recent four cell model proposed by Weaire and Phelan (1994) which outperforms the Kelvin foam model in terms of Kelvin's (1887) energetic optimality criterion requiring a minimum cell wall surface for a given cell volume.

The main disadvantage of structural foams is their disordered micro structure, leading to a distinct scatter in their effective material properties and thus to a limited reproducability of experimental measurements as well as theoretical predictions of their

* Corresponding author. Tel.: +49 761 5142 340; fax: +49 761 5142 401.
E-mail address: joerg.hohe@iwm.fraunhofer.de (J. Hohe).

0020-7683/$ - see front matter © 2008 Elsevier Ltd. All rights reserved.
doi:10.1016/j.ijsolstr.2008.10.008

material response. Especially in cases, where the characteristic micro and macro structural length scales do not differ by several orders of magnitude, as e.g. for metal foams with large cell sizes in the range of several millimeters used in sandwich structures with core thicknesses in the range of several centimeters, the probabilistic nature of the foam micro structure and thus the scatter in the effective properties are no longer negligible. In experimental studies by Blazy et al. (2004) as well as by Ramamurty and Paul (2004), it has been shown that uncertainty effects can be observed even for metal foams with less disordered micro structures. In this context, the most important stochastic parameter on the micro scale is the local relative density.

In order to account for the micro structural disorder of solid foams, a number of specialized homogenization approaches has been developed in the recent decade. Most of these studies are based on the computational generation and subsequent homogenization of a representative volume element with random micro structure using different versions of the Voronoï (1908) process. Approaches of this type have been used, among others, by Chen et al. (1999) for two-dimensional model foams featuring different types of imperfections, by Huyse and Maes (2001) or by Roberts and Garboczi (2002) who studied the effective elastic behavior of open cell foams where the occurrence of partially closed cell windows forms an additional micro structural geometric uncertainty. All of the mentioned approaches are based on a single analysis of a large scale representative volume element. Hence, they are capable to the determination of the mean macroscopic material response, whereas the scatter is not accessible. In order to assess the scatter, Shulmeister et al. (1998) as well as Zhu et al. (2000) performed a limited number of repeated executions of the generation and analysis of random computational models for foam micro structures using the Voronoï technique. The latter study also provides a first attempt for a systematic analysis of the effects of micro structural geometric uncertainties on the material uncertainties on the macroscopic level of structural hierarchy.

An alternative route to the use of the Voronoï (1908) procedure in its original and subsidary versions has been proposed by Daxner et al. (2000) as well as by Hohe and Becker (2005), using randomized regular foam models. In the latter study, a large number of repeated executions is employed to generate the stochastic information about the scatter which is assessed in terms of the basic stochastic parameters. As an alternative to the previously mentioned numerical approaches based on random number generation, Fortes and Ashby (1999) have proposed the use of direct probabilistic methods based on the analysis on the probability of the orientation of individual micro structural elements. Similar approaches have been used by Cuitiño and Zheng (2003) using a Taylor averaging technique and by Hall (1993) as well as by Warren and Kraynik (1997) using an orientation averaging approach based on the assumption of equal probability for all orientations of a simplified foam model in space.

For the homogenization analysis of randomly heterogeneous two-phase materials such as particle reinforced composites, a distinct body of literature exists. Among the numerous studies, only a few contributions should be mentioned which are of special interest for the problems the present study is concerned with. Ostoja-Starzewski (2006) has provided a comprehensive study on the size effect of the considered micro structural volume elements concerning different types of particle composites. Special interest is directed to the necessary size of the volume element in order to provide statistically representative results. A similar topic has been analyzed by Kanit et al. (2003) as well as by Lachihab and Sab (2005) concerning different types of particle aggregates. A comprehensive overview over concepts for homogenization of random media is provided in a recent book by Torquato (2002). Nevertheless, in the mechanics of foamed materials, rigorous stochastic methods have not widely been used.

Disadvantage of all approaches in the mechanics of foams mentioned previously is the problem that the scatter of the results and thus the uncertainty of the effective properties can only be assessed if the entire sequence of random generation of a computational model for the micro structure and the subsequent homogenization analysis is executed repeatedly in order to obtain the statistical information. In this context, it has to be noticed that the observed scatter strongly depends on the sample size due to self-averaging effects, resulting in the problem that for large samples the scatter can be predicted from the known scatter observed for small samples, whereas a reverse analysis is impossible. On the other hand, the use of small scale computational models for the micro structure with a limited number of pores might suppress a number of important interaction effects of neighboring cells such as the occurrence of a single large cell surrounded by a large number of cells much smaller in size due to the geometric restrictions.

In order to obtain the scatter on the lowest meaningful level and to circumvent the geometric restrictions imposed by the use of small computational foam models, the present study proposes an alternative approach for the probabilistic homogenization analysis of two-dimensional model foams, similar to the method used by Lachihab and Sab (2005) for particle composites. To avoid the restrictions of small scale models, a large scale, statistically representative volume element is employed. The corresponding random micro structure is generated by means of a Voronoï tesselation in Laguerre geometry (Fan et al., 2004) for which the best performance towards the reliable automatic generation of realistic foam models was observed. Subsequently, a finite element model for the micro structure is generated and its deformation behavior is analyzed under homogeneously distributed prescribed effective strain states. For evaluation purposes, the representative volume element is subdivided into a number of substructures consisting of a single cell wall intersection and half of the adjacent cell walls. For these substructures the effective stress and strain components are determined using a strain energy based homogenization concept. The results are evaluated statistically in terms of the resulting probability distributions for the local effective stress and strain components and the corresponding stochastic parameters.

2. Strain energy based homogenization procedure

The numerical homogenization of the foam micro structures in the present study is performed by means of a general strain energy based concept. Since the procedure has been derived and been employed previously (see Hohe and Becker, 2005), only a brief outline is presented here for a concise presentation.

Consider a mechanical body Ω according to Fig. 1. The body is assumed to be bounded by the external boundary $\partial\Omega^{\mathrm{u}} \cup \partial\Omega^{\mathrm{t}}$. On $\partial\Omega^{\mathrm{u}}$, the displacement components u_i are prescribed whereas the components $\sigma_{ij}n_j = t_i$ of the traction vector t_i are given on $\partial\Omega^{\mathrm{t}}$. In addition to the prescribed tractions t_i on the external surfaces, the body Ω might be loaded by distributed body loads f_i. The body is assumed to consist of a material with a cellular micro structure. For an efficient structural analysis on the effective level, the body Ω has to be replaced by a body Ω^* with the same shape and dimensions, bounded by the same external boundaries $\partial\Omega^{\mathrm{u}}$ and $\partial\Omega^{\mathrm{t}}$. The replacement body Ω^* has to be subject to similar distributed loads f_i^* as well as to similar prescribed surface tractions t_i^* and similar prescribed displacements u_i^* on the respective portions of the external surfaces as the original body Ω. In contrast to the original body Ω, the artificial replacement body Ω^* is assumed to consist of the quasi homogeneous "effective" medium with yet unknown properties.

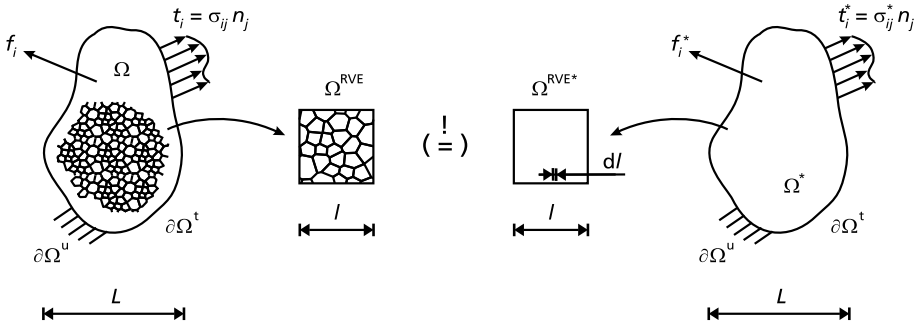

Fig. 1. Homogenization.

If the micro structure of the original body Ω does not explicitly depend on the spatial position within the body, at least in a statistical manner on the mesoscopic level of structural hierarchy, the consideration of a representative volume element Ω^{RVE} for the given micro structure is sufficient for determination of the properties of the quasi homogeneous effective medium. The characteristic dimension $l > dl$ of the representative volume element Ω^{RVE} has to be large enough so that the volume element is statistically representative for the entire micro structure of the body Ω in order to account for all possible micro structural effects. On the other hand, the dimension l of the representative volume element has to be smaller than the characteristic dimension L of the entire body Ω on the macroscopic level. The representative volume element Ω^{RVE} has to be replaced by a similar volume element Ω^{RVE*} consisting of the effective medium. In this context, the properties of the effective medium have to be chosen such that the mechanical response of the two volume elements Ω^{RVE} and Ω^{RVE*} is equivalent on the mesoscopic level of structural hierarchy.

Different conditions have been proposed for definition of the mesoscopic mechanical equivalence of the two volume elements Ω^{RVE} and Ω^{RVE*}. Within the approach used in the present study, it is assumed that the mechanical response of both volume elements is equivalent, if the average strain energy density

$$\bar{w} = \frac{1}{V^{RVE}} \int_{\Omega^{RVE}} w dV = \frac{1}{V^{RVE}} \int_{\Omega^{RVE*}} w^* dV = \bar{w}^* \tag{1}$$

in both volume elements is equal, provided that both volume elements are subject to a deformation which is mesoscopically equivalent. Mesoscopic equivalence of the deformation of both volume elements is assumed, if the volume averages

$$\overline{F}_{ij} = \frac{1}{V^{RVE}} \int_{\Omega^{RVE}} F_{ij} dV = \frac{1}{V^{RVE}} \int_{\Omega^{RVE*}} F_{ij}^* dV = \overline{F}_{ij}^* \tag{2}$$

of the components of the deformation gradient in both volume elements are equal. Subsequently, the effective stress and strain components can be determined from the components $\overline{F}_{ij} = \bar{u}_{i,j} + \delta_{ij}$ of the effective deformation gradient and the effective strain energy density $\bar{w}$ using their definitions on the mesoscopic level. Hence, the components of the effective Green-Lagrange strain tensor are given by

$$\bar{\gamma}_{ij} = \frac{1}{2}(\overline{F}_{ki}\overline{F}_{kj} - \delta_{ij}) \tag{3}$$

whereas the components of the effective second Piola-Kirchhoff stress tensor are defined by the derivative

$$\bar{\tau}_{ij} = \left.\frac{\partial \bar{w}}{\partial \bar{\gamma}_{ij}}\right|_{d\bar{\gamma}_{ij}^{pl}=0} \left(\approx \left.\frac{\Delta \bar{w}}{\Delta \bar{\gamma}_{ij}}\right|_{\Delta\bar{\gamma}_{ij}^{pl}=0} \right) \tag{4}$$

of the effective strain energy density with respect to the corresponding effective strain components. Alternatively, all other appropriate pairs of energy conjugate strain and stress measures might be used.

In its basic form, the numerical execution of the homogenization procedure defined by Eqs. (1)–(4) requires the following four steps:

- identification of an appropriate representative volume element,
- deformation of the representative volume element according to the effective deformation $\overline{F}_{ij}$ corresponding to the desired effective strain $\bar{\gamma}_{ij}$ linked by Eq. (3),
- computation of the average strain energy density $\bar{w}$ within the representative volume element for the desired effective strain state $\bar{\gamma}_{ij}$ and neighboring strain states $\bar{\gamma}_{ij} + \Delta\bar{\gamma}_{ij}$,
- computation of the effective stresses $\bar{\tau}_{ij}$ using Eq. (4).

In this context, the structural analysis of the representative volume element can be performed by any suitable method. Within the present study, the finite element method is employed.

3. Computational foam models

3.1. Division of space

For the random generation of computational models for the micro structure of solid foams, different strategies for the division of space have been proposed. Most of these procedures are based on a Voronoï (1908) tesselation of a representative volume element with different modifications. The Voronoï process is a two-step procedure. In the first step a number of nucleation points is generated at random spatial positions within the modeled volume or area. In the second step, the cellular micro structure is created from the positions of the nuclei.

In the original form of the Voronoï procedure, the spatial position of the nuclei is assumed to be uncorrelated so that each nucleation point can be positioned anywhere within the modeled area with an equal probability of each position. In the two-dimensional case, the cell belonging to the ith nucleation point $p^{(i)}$ at the spacial position $x_1^{(i)}$, $x_2^{(i)}$ is subsequently defined by all spacial points p at the positions x_1, x_2 for which the Euclidean distance

$$r_E(p, p^{(i)}) = \left(\left(x_1 - x_1^{(i)}\right)^2 + \left(x_2 - x_2^{(i)}\right)^2 \right)^{\frac{1}{2}} \tag{5}$$

is smaller than the Euclidean distance $r_E(p, p^{(j)})$ to all other nuclei $p^{(j)}$ with $i \neq j$. Thus, the area $A^{(i)}$ belonging to nucleation point $p^{(i)}$ is defined by

$$A(p^{(i)}) = \{p | p \in R^2, r_E(p, p^{(i)}) < r_E(p, p^{(j)}), j \neq i\}, \quad i,j = 1, \ldots, n \tag{6}$$

where n is the total number of nucleation points (see Fig. 2(a)). Without any additional constraining conditions, the Voronoï tesselation according to Eqs. (5) and (6) leads to a Γ-distribution of the cell size

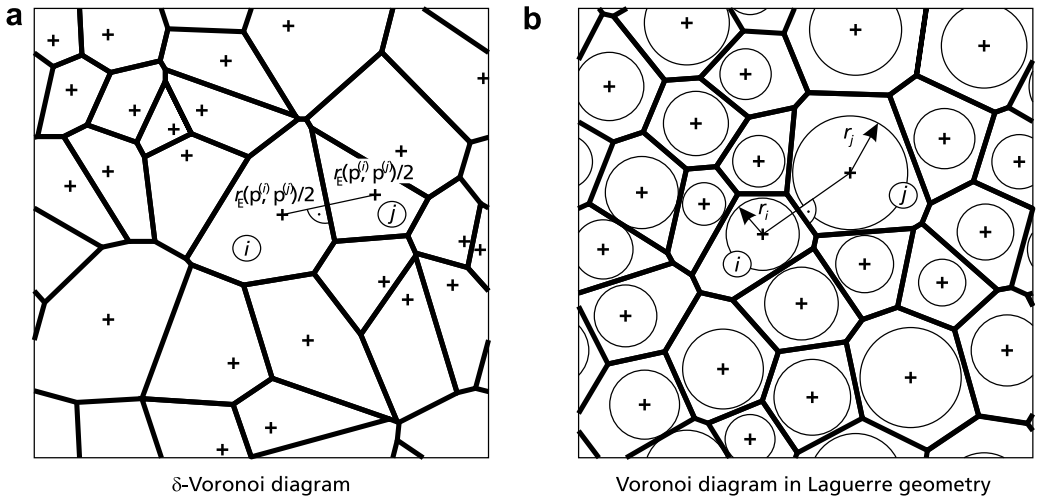

Fig. 2. Division of space.

instead of the experimentally observed logarithmic normal distribution (see Fan et al., 2004). Furthermore, due to the frequent occurrence of slender narrow cells, the obtained micro structures do not comply with Kelvin's (1887) optimality criterion requiring the development of a micro structure with the minimum possible cell surface.

A simple enhancement of the Γ-Voronoï process towards the generation of improved foam models is the introduction of a minimum permitted distance $r_{\mathrm{E}}^{\min} \leqslant r_{\mathrm{E}}(p^{(i)}, p^{(j)})$ between the individual nucleation points. This δ-Voronoï process in general generates improved computational models for the micro structure of solid foams. Nevertheless, the results are still suboptimal.

A distinct improvement is made by using a Voronoï tesselation in Laguerre geometry as proposed by Fan et al. (2004). The basic idea of this procedure consists in the use of the Laguerre distance

$$r_{\mathrm{L}}(p, p^{(i)}) = \left(r_{\mathrm{E}}(p, p^{(i)}))^2 - (r^{(i)*})^2\right)^{\frac{1}{2}} \tag{7}$$

instead of the Euclidean distance $r_{\mathrm{E}}(p, p^{(i)})$ defined by Eq. (5). In Eq. (7), the radii $r^{(i)*}$ define fixed circumcircles associated with the nucleation points $p^{(i)}$, which are not permitted to overlap (see Fig. 2(b)). In a similar manner as before, the area of the cell belonging to nucleus $p^{(i)}$ is defined by

$$A(p^{(i)}) = \{p | p \in R^2, r_{\mathrm{L}}(p, p^{(i)}) < r_{\mathrm{L}}(p, p^{(j)}),\ j \neq i\}, \quad i,j = 1, \ldots, n \tag{8}$$

where the Laguerre distance $r_{\mathrm{L}}(p, p^{(i)})$ according to Eq. (7) is used instead of its Euclidean counterpart $r_{\mathrm{E}}(p, p^{(i)})$. The Voronoï tesselation in Laguerre geometry in general provides reliable computational foam models in terms of Kelvin's (1887) energetic optimality criterion as well as in terms of the type of the cell size distribution.

In the present study, both, the δ-Voronoï tesselation as well as the Voronoï tesselation in Laguerre geometry are employed. In order to avoid difficulties with unrealsitic deformation constraints along the external boundaries of the representative volume elements, periodic micro structures are generated. For this purpose, n nucleation points are generated within the area of a rectangular representative volume element with the dimensions l_1 and l_2. Assuming that the entire micro structure consists of an infinite periodic array of similar volume elements, the nuclei are duplicated into the neighborhood of the modeled representative volume element shifting the positions of the duplicates by $\pm l_1$ and $\pm l_2$, respectively, into the eight neighboring volume elements of the infinite array forming the entire micro structure. In this context, care has to be taken in order to ensure that the distance constraints are also satisfied across the external boundaries of the volume elements. Subsequently, the cells forming the foam micro structure are generated by means of the respective procedure and the cell walls are cut at their intersections with the boundaries of the representative volume element with its neighborhood. Two examples for computational foam models generated by a periodic δ-Voronoï tesselation of the representative element and by a periodic Voronoï tesselation in Laguerre geometry consisting of 512 cells are illustrated in Fig. 3(a) and (b), respectively.

3.2. Finite element discretization

The structural analysis of the computational foam models is performed numerically using the finite element method. For this purpose, the foam micro structure is meshed by shear flexible Timoshenko beam elements with a linear interpolation of both, displacements and rotations. The beam elements are assumed to be of rectangular cross section with unit out-of-plane thickness and uniform thickness t within the x_1/x_2-plane. The thickness t is determined such that the prescribed relative density $\bar{\rho}$ of the foam structure is obtained. To ensure convergent results even in cases, where deformation localizations might develop, a maximum element length in the order of 10% of the average cell wall length is permitted. The material constitutive relation and the corresponding material parameters of the cell wall material are chosen according to the requirements of the specific type of foam under consideration. The numerical analysis is performed within the geometrically non linear framework, since large rotations of the individual struts of the foam will frequently develop under macroscopic loads in the compressive range due to buckling effects.

Assuming homogeneously distributed macroscopic reference strain states, the representative volume element is subjected to periodic boundary conditions. These conditions demand that the microscopic displacement gradients along corresponding external surfaces on opposite sides of the representative volume element have to be equal, ensuring micro structural continuity even in the deformed configuration. For the special case of a two-dimensional rectangular representative volume element with the dimensions l_1 and l_2 within the x_1- and x_2-directions, respectively, where the lower left corner coincides with the origin of the cartesian system x_i, the conditions

$$u_{i,1}|_{x_2=0} = u_{i,1}|_{x_2=l_2}, \quad i = 1,2 \tag{9}$$

$$\varphi_{3,1}|_{x_2=0} = \varphi_{3,1}|_{x_2=l_2} \tag{10}$$

$$u_{i,2}|_{x_1=0} = u_{i,2}|_{x_1=l_1}, \quad i = 1,2 \tag{11}$$

$$\varphi_{3,2}|_{x_1=0} = \varphi_{3,2}|_{x_1=l_1} \tag{12}$$

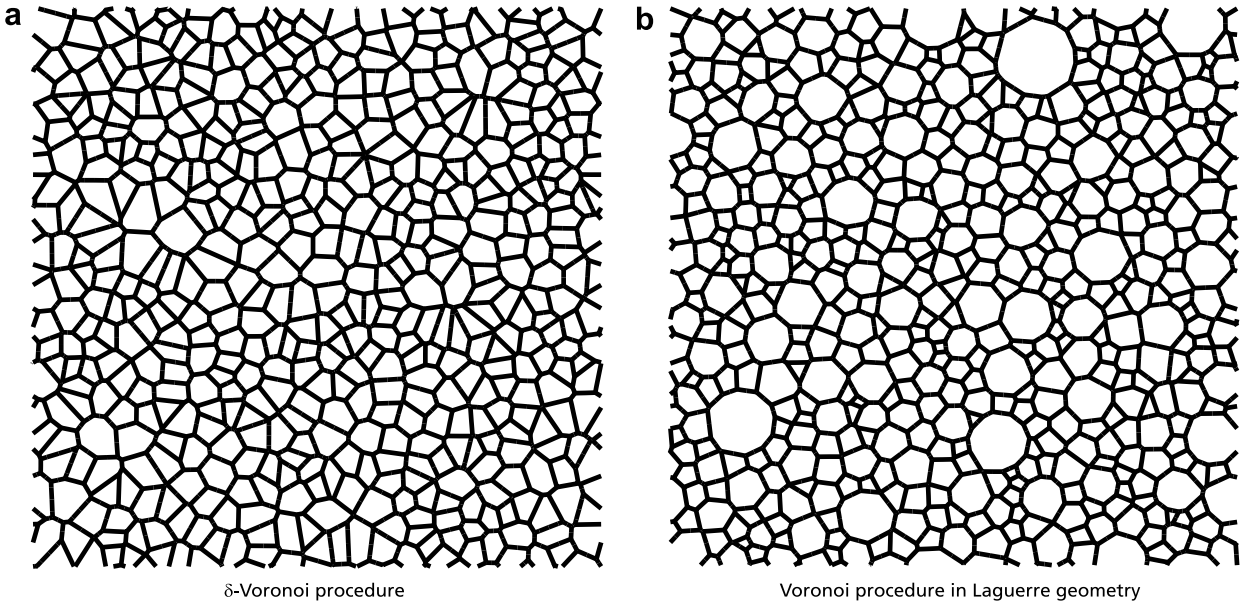

Fig. 3. Representative volume elements (512 cells).

have to be satisfied along the x_1- and x_2-parallel boundaries, respectively. For the use in the finite element analysis of the computational foam model, Eqs. (9)–(12) are rewritten to a discretized form by substituting the continuous partial derivatives with their numerical counterparts using finite differences between adjacent nodes on the external surfaces of the representative volume element.

For application within a finite elemet analysis, Eqs. (9)–(12) can be rewritten using the kinematic equivalence condition (2). Transformation of the area integral occurring in the two-dimensional equivalent of this condition into a boundary integral by means of Green's theorem yields

$$\overline{F}_{ij} = \frac{1}{A^{\mathrm{RVE}}} \int_{\partial A} u_i n_j \mathrm{d}s + \delta_{ij} \tag{13}$$

where n_j are the components of the outward normal unit vector on the boundary ∂A of the two-dimensional representative volume element. If the displacements and rotations between the boundary nodes are interpolated linearly, the integral in Eq. (13) can be evaluated resulting in the discrete periodic boundary conditions (see e.g. Hohe and Becker, 2005). Together with three additional conditions to constrain possible rigid body motions of the representative volume element, the discrete periodicity conditions form a complete set of displacement boundary conditions in terms of the components $\overline{F}_{ij}$ of the prescribed effective deformation gradient.

4. Local probabilistic approach

Previous approaches for the probabilistic analysis of the effective material properties of solid foams are either based upon the single analysis of large scale, statistically representative volume elements, or the repeated multiple analysis of small scale testing volume elements in a large number of numerical experiments. In the first case, only limited information is provided about the scatter and the uncertainty of the results whereas in the latter case, problems may arise due to the exclusive consideration of small scale, statistically non representative micro structures for which the occurrence of several long range effects such as the occurrence of single large cells surrounded by an excessive number of small cells might be suppressed by the computational modeling.

To comply with these problems, an alternative route is proposed in the present study. For this purpose a medium to large scale statistically representative volume element is considered. For the statistical evaluation the volume element is subdivided into a number of non representative small scale substructures or testing volume elements. Each of the testing volume elements consists of a single cell wall intersection and half of the three adjacent cell walls (see Fig. 4). Thus, the entire representative volume element is formed as the assembly of all testing volume elements. The testing volume elements defined in this manner provide the smallest reasonable structures for a homogenization analysis.

Based on the subdivision of the statistically representative volume element into the testing volume elements, a probabilistic homogenization analysis is performed, consisting of the following four steps:

- generation of an appropriate large scale computational foam model,
- numerical analysis of the deformation behavior of the representative volume element under a prescribed macroscopic state of deformation $\overline{F}_{ij}$ corresponding to a prescribed effective strain state $\bar{\gamma}_{ij}$,
- local homogenization analysis for determination of the local effective stress and strain states on the level of the testing volume elements,
- stochastic assessment of the results.

In the stochastic analysis, care has to be taken, since, due to their structure dependent definition, the testing volume elements intersected by the external surfaces of the representative volume element consist of two or more non consecutive parts located along opposite external surfaces. Since the testing volume elements defined according to Fig. 4 form the smallest meaningful substructures of the representative volume element, the proposed probabilistic homogenization procedure provides the stochastic information on the scatter in the effective material behavior on the lowest possible level. Alternatively, the probabilistic analysis of the scatter in the effective material response can be performed on higher levels, using testing volume elements of larger sizes, e.g. by combining adjacent testing volume elements.

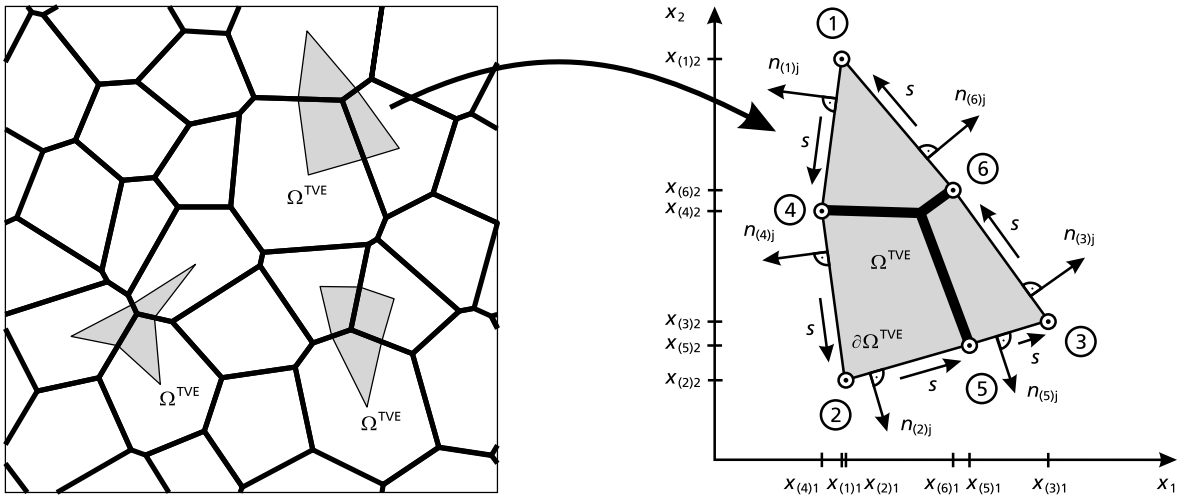

Fig. 4. Testing volume elements.

Within the probabilistic homogenization scheme, the local homogenization on the level of the testing volume elements is performed in a similar manner as for the entire representative volume element. According to Fig. 4, each testing volume element is defined by six nodes where the local nodes no. 4, 5 and 6 are the midside nodes of the corresponding cell walls. The dummy nodes no. 1, 2 and 3 are non structural nodes which have to be associated with the respective Voronoï cell in a unique manner. An appropriate definition for the position of a dummy-node is constituted by the weighted average of the positions of the cell wall intersections of the corresponding Voronoï cell. In this context, the position of each intersection is weighted by the length of the adjacent cell walls belonging to the considered Voronoï cell. In analogy, the displacements of the dummy nodes are defined as the weighted averages of the displacements of the respective cell wall intersections.

For each of the testing volume elements, the local effective stress and strain components are determined using a local version of Eqs. (1)–(4) and (13) related to the area Ω^{TVE} of the testing volume element instead of the area Ω^{RVE} of the entire representative volume element. For any externally applied macroscopic strain state $\bar{\gamma}_{ij}$, the corresponding local effective strain components $\bar{\gamma}_{ij}^{TVE}$ for all individual testing volume elements are determined by rewriting Eq. (13) into the form

$$\overline{F}_{ij}^{TVE} = \frac{1}{A^{TVE}} \int_{\partial\Omega^{TVE}} u_i n_j \mathrm{d}s + \delta_{ij} \tag{14}$$

defined on the testing volume element level. For each of the testing volume elements, the displacement components u_i along the boundaries of the testing volume element are interpolated linearly from the displacements of the local nodes 1 to 6 (see Fig. 4) which are determined in the finite element analysis of the entire representative volume element. Subsequently, the components $\overline{F}_{ij}^{TVE}$ of the local effective deformation gradient can be computed using Eq. (14). From the effective deformation gradient, the components $\bar{\gamma}_{ij}^{TVE}$ of the local effective Green-Lagrange strain tensor are obtained by using its definition (3).

Subsequently, the components $\bar{\tau}_{ij}^{TVE}$ of the local effective second Piola-Kirchhoff stress tensor are determined using Eq. (4). For purely hyperelastic materials without any dissipative effects, Eq. (4) can be rewritten as

$$\mathrm{d}\bar{w}^{TVE} = \bar{\tau}_{ij}^{TVE}\, \mathrm{d}\bar{\gamma}_{ij}^{TVE}, \quad i,j = 1,2 \tag{15}$$

on the testing volume element level. By substituting the infinitesimal increments $\mathrm{d}\bar{\gamma}_{ij}^{TVE}$ and $\mathrm{d}\bar{w}^{TVE}$ of the local effective strain components and the local effective strain energy density with their finite counterparts for a numerical evaluation, the approximate relation

$$\Delta\bar{w}^{TVE} \approx \bar{\tau}_{11}^{TVE}\Delta\bar{\gamma}_{11}^{TVE} + \bar{\tau}_{22}^{TVE}\Delta\bar{\gamma}_{22}^{TVE} + 2\bar{\tau}_{12}^{TVE}\Delta\bar{\gamma}_{12}^{TVE} \tag{16}$$

is obtained for the two-dimensional case.

In order to employ Eq. (16) for determination of the local effective stress components $\bar{\tau}_{ij}^{TVE}$, the change $\Delta\bar{w}^{TVE}$ of the average strain energy density of the respective testing volume element in the case of changes $\Delta\bar{\gamma}_{ij}^{TVE}$ has to be computed. For this purpose, the average strain energy density $\bar{w}^{TVE}$ and the local effective strain components $\bar{\gamma}_{ij}^{TVE}$ for each testing volume element are determined for the considered (applied) macroscopic effective strain state $\bar{\gamma}_{ij}^{(0)}$ as well as for three neighboring strain states

$$\bar{\gamma}_{ij}^{(k)} = \bar{\gamma}_{ij}^{(0)} + \Delta\bar{\gamma}_{ij}^{(k)}, \quad k = 1,2,3 \tag{17}$$

which have to be linearly independent from each other. For each of the macroscopic strain states, the corresponding local effective strain components $\bar{\gamma}_{ij}^{TVE(k)}$ as well as the local average strain energy densities $\bar{w}^{TVE(k)}$ with $k = 0,\ldots,3$ are computed. Subsequently, the finite differences

$$\Delta\bar{\gamma}_{ij}^{TVE(k)} = \bar{\gamma}_{ij}^{TVE(k)} - \bar{\gamma}_{ij}^{TVE(0)}, \quad k = 1,2,3 \tag{18}$$

$$\Delta\bar{w}^{TVE(k)} = \bar{w}^{TVE(k)} - \bar{w}^{TVE(0)}, \quad k = 1,2,3 \tag{19}$$

for the local effective stain components $\bar{\gamma}_{ij}^{TVE}$ and the corresponding local average strain energy density $\bar{w}^{TVE}$ are computed. Since Eq. (16) has to be satisfied for all three differences $\Delta\bar{w}^{TVE(k)}$, the following system of equations is obtained:

$$\begin{pmatrix} \Delta\bar{\gamma}_{11}^{TVE(1)} & \Delta\bar{\gamma}_{22}^{TVE(1)} & 2\Delta\bar{\gamma}_{12}^{TVE(1)} \\ \Delta\bar{\gamma}_{11}^{TVE(2)} & \Delta\bar{\gamma}_{22}^{TVE(2)} & 2\Delta\bar{\gamma}_{12}^{TVE(2)} \\ \Delta\bar{\gamma}_{11}^{TVE(3)} & \Delta\bar{\gamma}_{22}^{TVE(3)} & 2\Delta\bar{\gamma}_{12}^{TVE(3)} \end{pmatrix} \begin{pmatrix} \bar{\tau}_{11}^{TVE} \\ \bar{\tau}_{22}^{TVE} \\ \bar{\tau}_{12}^{TVE} \end{pmatrix} = \begin{pmatrix} \Delta\bar{w}^{TVE(1)} \\ \Delta\bar{w}^{TVE(2)} \\ \Delta\bar{w}^{TVE(3)} \end{pmatrix} \tag{20}$$

By a solution of this system, the corresponding local effective stress components $\bar{\tau}_{ij}^{TVE}$ corresponding to the local effective strain state $\bar{\gamma}_{ij}^{TVE} = \bar{\gamma}_{ij}^{TVE(0)}$ are obtained.

In the case of a linear elastic cell wall material and small deformations, the analysis of the effective material response in terms of the local effective stress–strain response defiend by the Green-Lagrange strain components $\bar{\gamma}_{ij}^{TVE}$ and the corresponding local effective second Piola-Kirchhoff stress components $\bar{\tau}_{ij}^{TVE}$ can be replaced by a simplified analysis in terms of the components $\overline{C}_{ij}^{TVE}$ of the local effective stiffness matrix interrelating the effec-

tive local Cauchy stress components $\bar{\sigma}_{ij}^{\mathrm{TVE}}$ with the local effective components $\bar{\varepsilon}_{ij}^{\mathrm{TVE}}$ of the infinitesimal strain tensor according to

$$\begin{pmatrix} \bar{\sigma}_{11}^{\mathrm{TVE}} \\ \bar{\sigma}_{22}^{\mathrm{TVE}} \\ \bar{\sigma}_{12}^{\mathrm{TVE}} \end{pmatrix} = \begin{pmatrix} \overline{C}_{11}^{\mathrm{TVE}} & \overline{C}_{12}^{\mathrm{TVE}} & \overline{C}_{16}^{\mathrm{TVE}} \\ & \overline{C}_{22}^{\mathrm{TVE}} & \overline{C}_{26}^{\mathrm{TVE}} \\ (\mathrm{sym.}) & & \overline{C}_{66}^{\mathrm{TVE}} \end{pmatrix} \begin{pmatrix} \bar{\varepsilon}_{11}^{\mathrm{TVE}} \\ \bar{\varepsilon}_{22}^{\mathrm{TVE}} \\ 2\bar{\varepsilon}_{12}^{\mathrm{TVE}} \end{pmatrix}. \tag{21}$$

In this case the local average strain energy density is directly related with the local effective stress and strain components by

$$\bar{w}^{\mathrm{TVE}} = \frac{1}{2}\bar{\sigma}_{ij}^{\mathrm{TVE}}\bar{\varepsilon}_{ij}^{\mathrm{TVE}}. \tag{22}$$

Substituting the stress components in this expression with Eq. (21) yields an expression for the local average strain energy density in terms of the local effective strain components $\bar{\varepsilon}_{ij}^{\mathrm{TVE}}$ and the local effective stiffness components $\overline{C}_{ij}^{\mathrm{TVE}}$. Based on this expression, similar to Eq. (20), a linear system of equations can be derived for the local effective stiffness components, if six linearly independent macroscopic strain states are considered.

Care has to be taken when solving this system or the system (20) since the conditioning of the respective matrices can be poor in cases, where similar local effective strain states develop even for independent applied macroscopic strain states due to the activation of energetically preferred local states of deformation as it might happen especially in the postbuckling range under compressive external loading conditions. To avoid problems with the resulting "noisy" solutions, an adaptive scheme is used, where prior to the solution of the respective system, the conditioning of the matrices is checked. In cases where large condition numbers indicate the risk of non feasable, numerically unstable solutions, an alternative set of macroscopic effective strain states is applied.

The stochastic assessment of the results on the local effective stress and strain components $\bar{\tau}_{ij}^{\mathrm{TVE}}$ and $\bar{\varepsilon}_{ij}^{\mathrm{TVE}}$ (or the effective stiffness components $\overline{C}_{ij}^{\mathrm{TVE}}$) is performed in terms of the corresponding cumulative probability distributions $F(x)$ where x is the respective random variable. For determination of the (cumulative) probability distributions, the numerical results of the respective random variable (local effective strain, stress or stiffness component) are rearranged into ascending order. Subsequently, a cumulative probability of

$$F(x_i) = \frac{i - \frac{1}{2}}{q}, \quad i = 1, \ldots, q \tag{23}$$

where q is the total number of values for the random variable is assigned to the ordered set of variables x_i. The corresponding probability density distributions would be obtained as the partial derivatives of the probability distributions with respect to the random variable. In addition, the average of the mechanical field quantity under consideration and the corresponding scatter can be assessed in terms of the expectation value

$$E(x) = \sum_{i=1}^{q} x_i P(x_i) \tag{24}$$

and the variance

$$V(x) = \sum_{i=1}^{q} (E(x) - x_i)^2 P(x_i) \tag{25}$$

respectively, where $P(x_i)$ is the individual probability for the occurrence of the result x_i. Assuming a uniform distribution for the individual data x_i, an equal individual probability of $P(x_i) = 1/q$ is assigned to all x_i. As the first moment and the second central moment of the probability distribution, the expectation value $E(x)$ and the Variance $V(x)$ form the most important stochastic parameters.

5. Results

5.1. Convergence

Prior to the application of the probabilistic homogenization scheme proposed in Section 4, a study of convergence concerning the necessary number of Voronoï cells is performed. For this purpose, different computational foam models with a total number of $q = 16$, 32, 64, 128, 256 and 512 cells are generated using the Voronoï tesselation in Laguerre geometry. The foam models are subjected to three different effective strain states on the macroscopic level, including a uniaxial compresive strain state with $\bar{\gamma}_{11} = -0.025$, a uniaxial tensile strain state with a larger applied strain level of $\bar{\gamma}_{11} = 0.1$ and a pure shear strain state with $\bar{\gamma}_{12} = 0.05$. All other effective strain components are assumed to vanish. The analysis is performed within the geometrically non-linear framework assuming an Ogden-type hyperelastic material on the cell wall level.

The results for the three different applied strain states are presented in Fig. 5(a) to (c), respectively. In all three figures, the probability distribution $F(\bar{\gamma}_{ij}^{\mathrm{TVE}})$ of the local effective strain component $\bar{\gamma}_{ij}^{\mathrm{TVE}}$ corresponding to the non-vanishing component $\bar{\gamma}_{ij}$ of the respective applied strain state is plotted as a function of the local effective strain component. In all three cases, rough estimates of the probability distributions can be obtained with small numbers q of Voronoï cells in the computational foam models. For medium numbers q, these estimates might already be sufficient for a convergent analysis of the expectation values $E(\bar{\gamma}_{ij}^{\mathrm{RVE}})$ and the corresponding variances $V(\bar{\gamma}_{ij}^{\mathrm{RVE}})$. Nevertheless, sufficienty smooth graphs of the probability distributions require cell numbers of $q = 500$ or beyond. Similar results are obtained for the probability distributions related to the other local effective strain components $\bar{\gamma}_{ij}^{\mathrm{TVE}}$ and the corresponding local effective stress components $\bar{\tau}_{ij}^{\mathrm{TVE}}$.

Hence, all subsequent computations, whether based on a Voronoï tesselation in Laguerre geometry or a δ-Voronoï tesselation are performed with a number of 512 Voronoï cells and thus 1024 testing volume elements. The corresponding model sizes are sufficiently large in order to guarantee the occurrence of all essential micro structural features within the representative volume element. On the other hand, with this model size, the analyses can still be performed in a numerically rather efficient manner. Examples for the corresponding micro structures consisting of 512 Voronoï cells obtained by a δ-Voronoï tesselation and a Voronoï tesselation in Laguerre geometry have been presented in Fig. 3(a) and (b), respectively.

5.2. Effective stiffness components

In a first application, the proposed local probabilistic homogenization scheme is applied to an analysis of uncertainty effects in the effective stiffness components of linear elastic foams. As a cell wall material, aluminum with a Young's modulus of $E = 70$ GPa and a Poisson's ratio of $\nu = 0.3$ is assumed. Based on the results of the study of convergence described in Section 5.1, the computational model of the micro structure is generated by means of a Voronoï tesselation in Laguerre geometry, using 512 cells. The parameters of the underlying prescribed size distribution of the circular areas associated with the individual nuclei are varied so that a wide range of micro structural degrees of disorder is investigated. As a measure for the micro structural degree of disorder, the variance $V(A/A_0)$ of the cell size A normalized with the average cell size $A_0 = A^{\mathrm{RVE}}/n$ is employed. The cell wall thickness is adapted such that a constant relative density of $\bar{\rho} = 0.05$ (average over the entire representative volume element) is obtained for all computational foam models in the study.

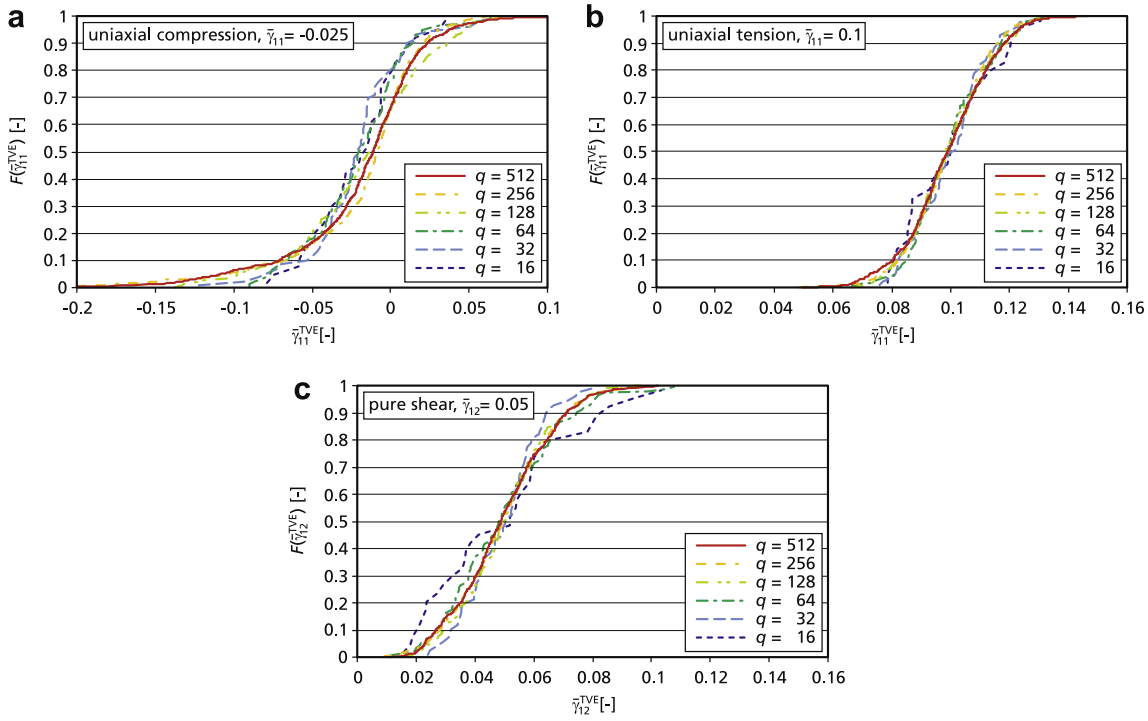

Fig. 5. Study of convergence: (a) uniaxial compressive strain, (b) uniaxial tensile strain and (c) pure shear strain.

The resulting probability distributions $F(\overline{C}_{ij}^{TVE})$ of the non vanishing normal stiffness components $\overline{C}_{11}^{TVE}$ and $\overline{C}_{22}^{TVE}$, the in-plane coupling stiffness $\overline{C}_{12}^{TVE}$ as well as the shear stiffness $\overline{C}_{66}^{TVE}$ according to Eq. (21) are presented in Fig. 6(a) to (d), respectively. Three different degrees $V(A/A_0)$ of micro structural disorder are considered, ranging from medium to highly disordered foams. The expectation value $E(\overline{C}_{ij}^{TVE})$ and the variance $V(\overline{C}_{ij}^{TVE})$ of the non vanishing stiffness components are presented in Fig. 7(a) to (d), respectively, in dependence on the degree $V(A/A_0)$ of micro structural disorder. In addition, a comparison of the results based on computational models obtained by a Voronoï tesselation in Laguerre geometry with results based on models obtained by a δ-Voronoï process is included in Fig. 7.

For all four non vanishing effective stiffness components $\overline{C}_{ij}^{TVE}$, high levels of uncertainty indicated by distinct scatter band widths are observed even for medium or low degrees $V(A/A_0)$ of micro structural disorder (see Fig. 6). In the case of the normal stiffness components $\overline{C}_{11}^{TVE}$ and $\overline{C}_{22}^{TVE}$, the wide range of the individual stiffness values is caused by the activation of different deformation mechanisms on the microscopic level. For testing volume elements with preferred cell wall orientation within the loading direction, the microscopic mechanism of deformation consists mainly of stretching of the cell walls within their longitudinal direction. Since cell wall stretching is a mode of deformation involving high local strain energy densities, a stiff behavior of the corresponding elements is obtained. If, on the other hand, the cell walls of a specific testing volume element are preferrably orientated perpendicular to the loading direction, a soft effective behavior is obtained due to the activation of a microscopic mode of deformation related mainly to cell wall bending and thus requiring low amounts of work for significant deflections. Especially for micro structures featuring high levels of micro structural disorder, the probability of the occurrence of testing volume elements with extreme orientation of their micro structure increases resulting in the observed large scatter band widths. On the other hand, the expectation values of the normal stiffness components $\overline{C}_{11}^{TVE}$ and $\overline{C}_{22}^{TVE}$ are not affected by the micro structural disorder in terms of increasing variances $V(A/A_0)$ of the cell size distribution as it is observed in Figs. 6 and 7(a) and (b), respectively.

A contrary observation can be made for the in-plane coupling stiffness $\overline{C}_{12}^{TVE}$ where an increasing micro structural disorder leads not only to an increasing scatter band width but also to a decreasing expectation value $E(\overline{C}_{12}^{TVE})$. In a similar manner, the expectation value $E(\overline{C}_{66}^{TVE})$ and thus the mean effective shear stiffness increases with increasing degree $V(A/A_0)$ of micro structural disorder. For increasingly disordered micro structures, the probability of cell wall orientations which require longitudinal stretching or compression under macroscopic shear deformation increases. Thus, the average effective shear stiffness increases with an increasing variance of the cell size distribution, compared to the extreme case of a perfectly regular hexagonal micro structure, where the underlying micro structural mechanism of deformation would be pure cell wall bending as it has been shown by Gibson and Ashby (1997).

Especially for the case of the effective local shear stiffness $\overline{C}_{66}^{TVE}$ and, in a limited manner, for the in-plane effective local coupling stiffness $\overline{C}_{12}^{TVE}$, asymmetric probability distributions $F(\overline{C}_{ij}^{TVE})$ are observed (see Fig. 6), featuring an increasing skewness with increasing degree of micro structural disorder. This effect emphasizes that a probabilistic assessment in terms of the expectation or mean value $E(x)$ and variance $V(x)$ or the standard deviation alone might be insufficient, since the underlying probability distributions are essentially not of the Gaussian type and hence cannot be characterized completely in terms of two the basic probabilistic parameters.

For a further assessment of the strategies for the division of space used for the generation of the computational foam models, results based on foam models based on a δ-Voronoï tesselation are added to Fig. 7. For low degrees of micro structural disorder, the results prove to be identical to the results based on the favored Voronoï tesselation in Laguerre geometry. On the other hand, increasing differences between the results based on the two competing space division strategies are observed in all cases, where the respective stochastic parameters $E(\overline{C}_{ij}^{TVE})$ and $V(\overline{C}_{ij}^{TVE})$ are dependent on the degree $V(A/A_0)$ of micro structural disorder. In this context, strong effects are observed especially for the variances. Neverthe-

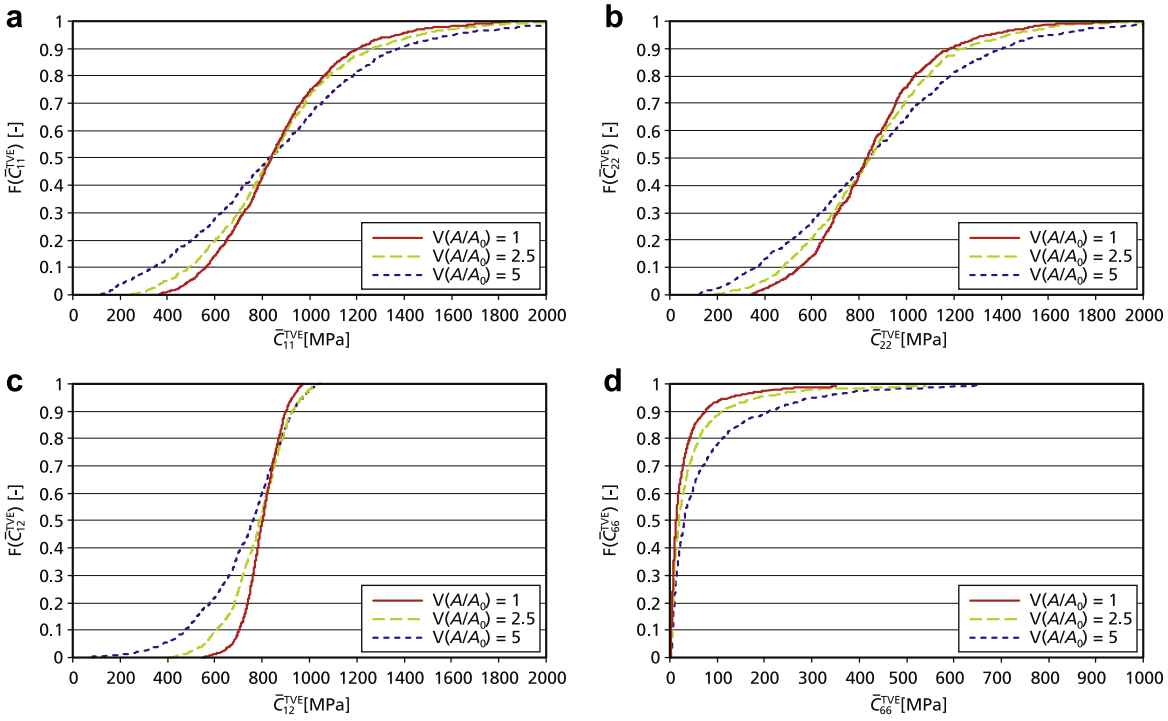

Fig. 6. Local effective stiffness components, probability distributions: (a) normal stiffness C_{11}, (b) normal stiffness C_{22}, (c) normal coupling stiffness C_{12} and (d) shear stiffness C_{66}.

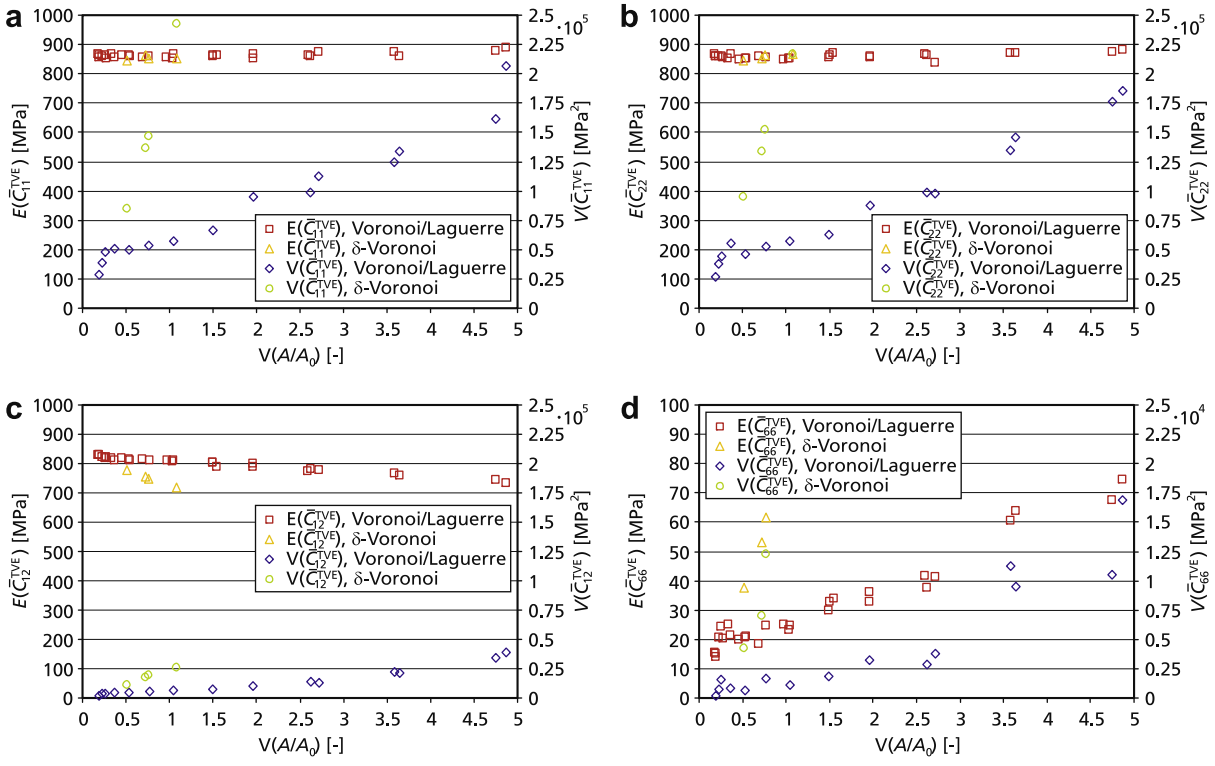

Fig. 7. Local effective stiffness components, expectation values and variances: (a) normal stiffness C_{11}, (b) normal stiffness C_{22}, (c) normal coupling stiffness C_{12} and (d) shear stiffness C_{66}.

less, although distinct effects are definitely present, it should be noticed that the increase would be less dramatic, if the standard deviation as the square root of the variance would have been used instead.

In order to investigate the reasons for the different results obtained for both space division strategies, a more detailed comparison is made for the case of two specific micro structures, featuring an identical degree of micro structural disorder in terms of the

variance of the cell size distribution. The micro structures of the representative volume elements are presented in Fig. 8(a) and (b), respectively. As it is observed in Fig. 8(c), both micro structures feature an identical cell size distribution except some minor scattering differences caused by the fact that a finite number of $q = 512$ cells is used. Nevertheless, although the cell size distribution of both computational foam models is identical, distinct differences are observed in terms of the probability distributions of the local relative density presented in Fig. 8(d) where the scatter band width for the structure generated by the δ-Voronoï procedure is approximatly twice of the scatter band width for the structure generated by means of a Voronoï tesselation in Laguerre geometry. This effect is caused by the occurrence of a non negligible number of unrealistically slender narrow cells in case of the model generated by the δ-Voronoï process (see Fig. 8(a)), resulting in an inferior performance of the δ-Voronoï process in terms of Kelvin's (1887) energetic optimality criterion compared to the Voronoï process in Laguerre geometry. The presence of these cells leads to an increasing overall summed up length of the cell walls and thus, in conjunction with the prescribed fixed average relative density to a decreased cell wall thickness. Furthermore, the local mechanical behavior of the slender and narrow cells is strongly anisotropic and thus causes an addtional scatter in the local effective material response. Hence, care has to be taken in the choice of the procedure to be employed for the generation of computational models of structural foams.

5.3. Non linear elastic material response

The local effective stresses are governed by the local effective stiffnesses in conjunction with the local effective strains. Hence, the scatter of the local effective stresses is governed by the scatter in the local effective stiffness as it is analyzed in Section 5.2 for the case of linear elastic cell wall materials together with the scatter in the local effective strains. Furthermore, the effective stiffness and the effective strains in general are correlated random variables due to equilibrium requirements for the stresses (or the stress resultants) on the microscopic level. Therefore, the effective stresses are investigated in more detail in the following section.

As in Section 5.2, the computational models for the two-dimensional foam micro structure are generated by means of a Voronoï tesselation in Laguerre geometry using a total of 512 cells and thus 1024 testing volume elements in the modeled part of the micro structure forming the representative volume element. Different degrees of micro structural disorder are considered by different choices of the parameters governing the size distribution of the original circular cells associated with the individual nucleation points. To enable a direct comparability of the results for different levels of disorder, a unique average relative density of $\bar{\rho} = 0.05$ for the representative volume elements is employed, adapting the cell wall thickness accordingly.

In order to account for geometry changes especially in the high compression range, the analyses are performed within the geometrically non linear framework. On the cell wall level, a compressible Ogden-type hyperelastic material model is assumed. The strain energy potential of this model is given by

$$w = \sum_{k=1}^{n} \frac{\mu_{(k)}}{\alpha_{(k)}} \left((\lambda_1^{\mathrm{dev}})^{\alpha_{(k)}} + (\lambda_2^{\mathrm{dev}})^{\alpha_{(k)}} + (\lambda_3^{\mathrm{dev}})^{\alpha_{(k)}} - 3 \right) + \sum_{k=1}^{n} \kappa_{(k)} (J-1)^{2k} \tag{26}$$

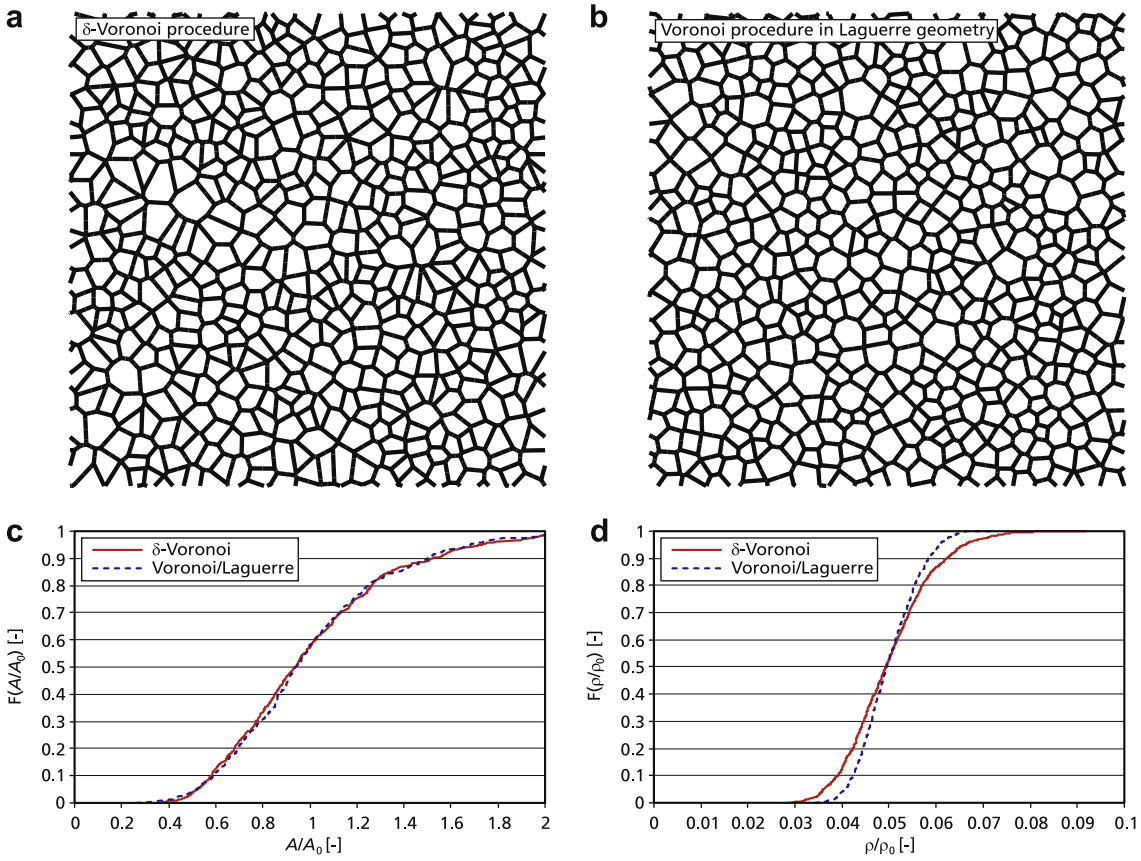

Fig. 8. Comparison of δ-Voronoï procedure and Voronoï procedure in Laguerre geometry: (a) δ-Voronoï tesselation, (b) Voronoï tesselation in Laguerre geometry, (c) cell size distributions and (d) probability distribution of the local relative density.

with

$$\lambda_k^{\mathrm{dev}} = J^{-\frac{1}{3}}\lambda_k \tag{27}$$

where λ_k are the principal values of the deformation gradient whereas J denotes the corresponding Jacobian. Within the Ogden material model (26), the quantities n and $\alpha_{(k)}$ as well as the generalized shear and compression moduli $\mu_{(k)}$ and $\kappa_{(k)}$, respectively are material constants ($k = 1,\ldots,n$). Throughout the present study, the material parameters are assumed as $n = 2$ with $\alpha_1 = 2$, $\mu_1 = 0.5\mathrm{GPa}$ and $\kappa_1 = 0.6\mathrm{GPa}$ as well as $\alpha_2 = -2$, $\mu_2 = -0.1\mathrm{GPa}$ and $\kappa_2 \approx \infty$. The material response defined by these parameters is within the range regarded as typical for polymeric materials. For small and moderate deformations, an approximately linear uniaxial microscopic material response is obtained.

The effective material response of the foamed micro structures is analyzed under uniaxial tensile and compressive prescribed effective strain states $\bar{\gamma}_{ij}$. The results are evaluated in terms of the local effective second Piola-Kirchhoff stress and Green-Lagrange strain components $\bar{\tau}_{ij}^{\mathrm{TVE}}$ and $\bar{\gamma}_{ij}^{\mathrm{TVE}}$, respectively. Due to the statistically non representative character of the testing volume elements, strong variations of the local stress strain response are present on the mesoscopic level. In Fig. 9, the effective global stress strain characteristics on the level of the entire representative volume element as well as the local effective stress strain curves for an arbitrarily chosen subset of four out of 1024 testing volume elements are presented. Fig. 9(a) is related to uniaxial compression, whereas the stress strain characteristics for uniaxial tensile deformation are presented in Fig. 9(b). In the latter, the slope of the individual curves is defined by the stiffness whereas the individual maximum strain level, which is in all cases related to the maximum level of $\bar{\gamma}_{11} = 0.25$ of the applied effective macroscopic strain, is an indicator for the uncertainty in the local effective strain state. Although only a rather small subset out of the overall set of results is presented, the correlation of the local effective stiffness and the local effective strain level is quantitatively obvious since steeper local stress strain curves tend to smaller local strain levels indicated by the final point of the respective curves.

The observed distinct differences in the effective stiffness of the individual testing volume elements are caused by the activation of different mechanisms of deformation on the microscopic level, depending on the geometry of the respective testing volume element (see Section 5.2). A stiff behavior is obtained for testing volume elements with a preferred orientation of the cell walls within the macroscopic loading direction, since for these cases, longitudinal stretching (or compression) involving large amounts of work for a specific deformation is the dominant microscopic mechanism of deformation. For testing volume elements with a predominant cell wall orientation perpendicular to the macroscopic loading direction, low energy cell wall bending modes are the dominant micro structural mechanisms of deformation resulting in a weaker response. Under compression, the situation becomes more complex, since in addition to the micro structural modes of deformation defined by longitudinal cell wall stretching and transverse cell wall bending, instabilities due to cell wall buckling develop. In this context, strong interaction effects between neighboring testing volume elements have to be expected, since the development of instability effects in neighboring testing volume elements during the loading history may result in a rapid change in the loading situation of the considered testing volume element. Hence, in addition to the high level of uncertainty in the stresses belonging to a specific prescribed strain state on the macroscopic level, multiple kinks are observed in the local effective stress strain characteristics presented in Fig. 9(a).

In order to investigate the effect of the micro structural disorder on the effective material response in more detail, the effective stress and strain components at different selected macroscopic strain levels are investigated. In Fig. 10(a) and (b), the probability distributions $F(\bar{\gamma}_{ij}^{\mathrm{TVE}})$ of the local effective strain components $\bar{\gamma}_{11}^{\mathrm{TVE}}$ within the macroscopic loading direction and $\bar{\gamma}_{22}^{\mathrm{TVE}}$ perpendicular to the macroscopic loading direction are presented for an uniaxial macroscopic tensile state of deformation with an applied effective strain of $\bar{\gamma}_{11} = 0.025$. The probability distributions of the local effective stress components $\bar{\tau}_{11}^{\mathrm{TVE}}$ and $\bar{\tau}_{22}^{\mathrm{TVE}}$ within and perpendicular to the direction of the applied macroscopic strain are presented in Fig. 10(c) and (d), respectively. In all cases, three different degrees of micro structural disorder are considered, ranging from a medium level of disorder with $V(A/A_0) = 1$ up to a high level with $V(A/A_0) = 5$. In Fig. 11(a) to (d), corresponding expectation values and variances are presented directly as functions of the micro structural disorder characterized by the variance $V(A/A_0)$ of the cell size distribution.

The expectation values $E(\bar{\gamma}_{ij}^{\mathrm{TVE}})$ of the local effective strains within and perpendicular to the macroscopic loading direction coincide with the corresponding values of the applied macroscopinc effective strains with $\bar{\gamma}_{11} = 0.025$ and $\bar{\gamma}_{22} = 0$, respectively. As expected, no effect of the micro structural disorder is observed. The scatter of both local effective strain components increases moderately with increasing micro structural disorder due to the increasing probability of the presence of testing volume elements where either the stretching or the bending mechanism is the predominant micro structural mechanism of deformation. Consequently, the scatter band width increases.

For the corresponding effective stress components $\bar{\tau}_{11}^{\mathrm{TVE}}$ and $\bar{\tau}_{22}^{\mathrm{TVE}}$ acting within and perpendicular to the macroscopic loading direction, respectively, stronger effects are observed. Especially, the expectation values $E(\bar{\tau}_{ij}^{\mathrm{TVE}})$ tend to decrease with increasing micro structural disorder. Hence, the geometric uncertainty of the micro structure does not only affect the scatter of the effective stresses

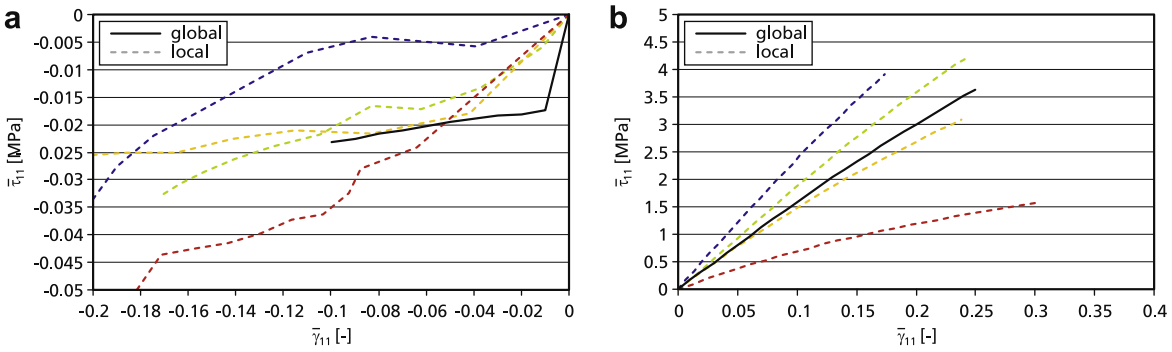

Fig. 9. Effective global and local stress strain response: (a) uniaxial compressive and (b) uniaxial tensile deformation.

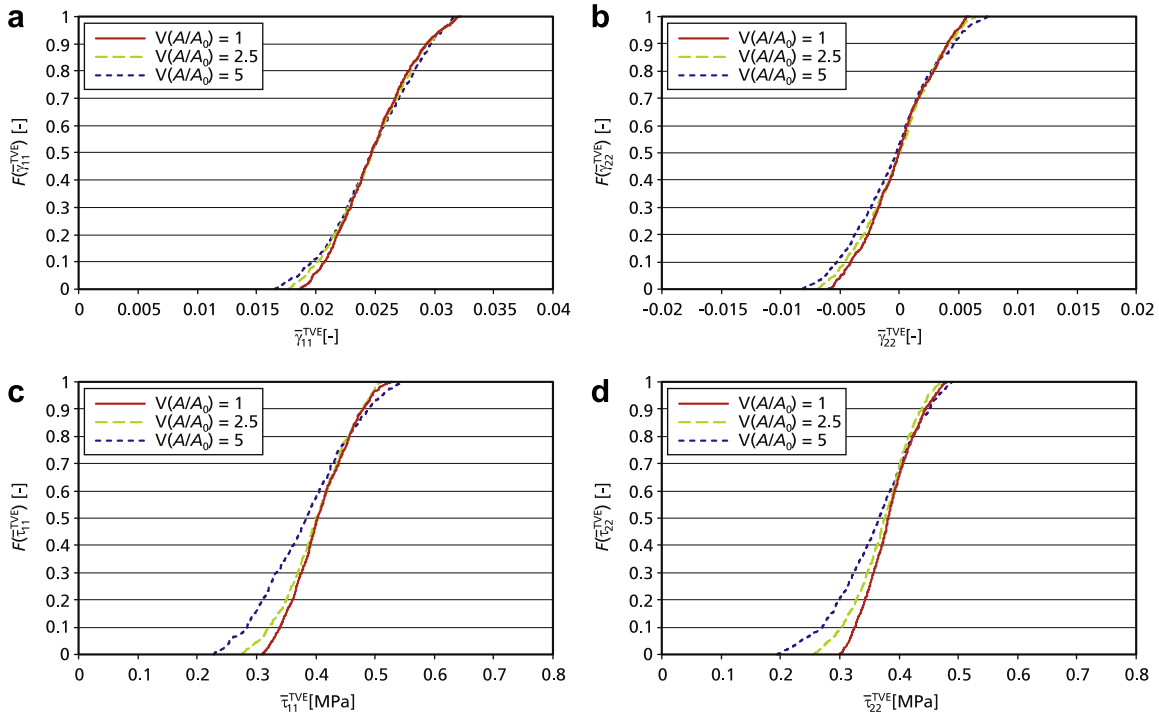

Fig. 10. Effective local strain and stress components in tension, probability distributions: (a) Green-Lagrange normal strain $\bar{\gamma}_{11}$ within the global straining direction, (b) Green Lagrange normal strain $\bar{\gamma}_{22}$ perpendicular to the global straining direction, (c) second Piola-Kirchhoff stress $\bar{\tau}_{11}$ within the global straining direction and (d) second Piola-Kirchhoff stress $\bar{\tau}_{22}$ perpendicular to the global straining direction.

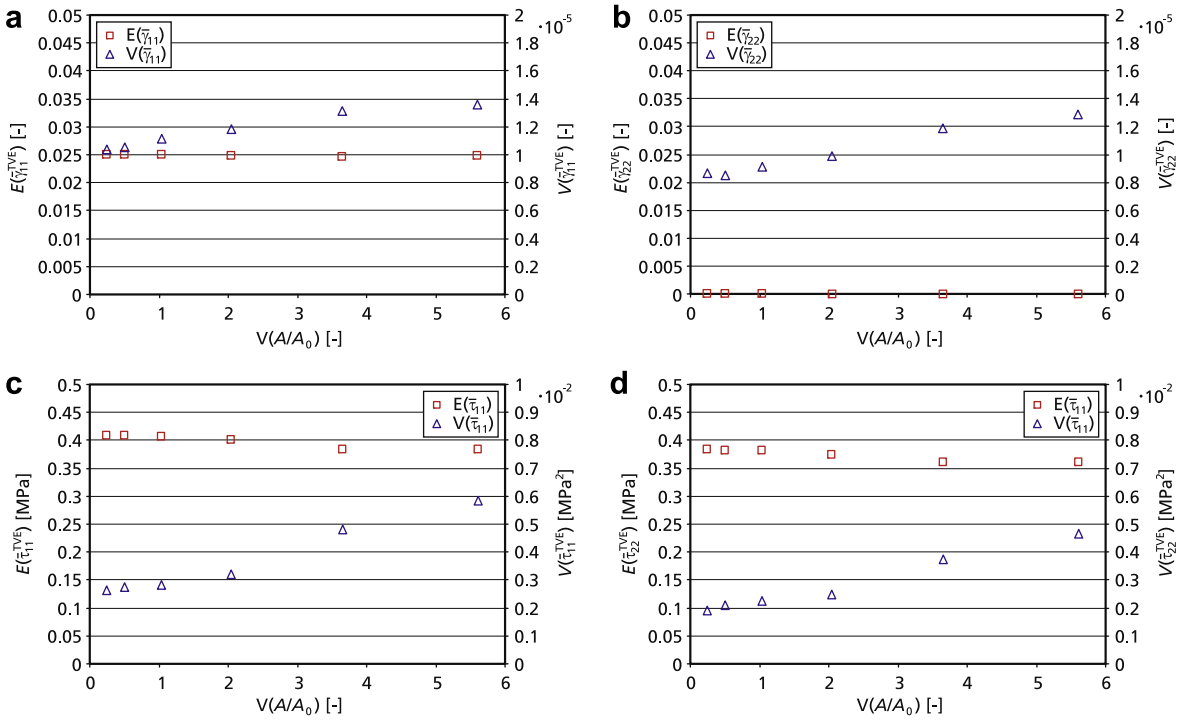

Fig. 11. Effective local strain and stress components in tension, expectation values and variances: (a) Green-Lagrange normal strain $\bar{\gamma}_{11}$ within the global straining direction, (b) Green Lagrange normal strain $\bar{\gamma}_{22}$ perpendicular to the global straining direction, (c) second Piola-Kirchhoff stress $\bar{\tau}_{11}$ within the global straining direction and (d) second Piola-Kirchhoff stress $\bar{\tau}_{22}$ perpendicular to the global straining direction.

but also influences the corresponding excpectation or mean values, as it has been observed in previous studies (Hohe and Becker, 2005). Consequently, the probability distributions $F(\bar{\tau}_{ij}^{\mathrm{TVE}})$ presented in Fig. 10(c) and (d) are shifted towards smaller stress levels for increasing levels of disorder. Increasing variances $V(\bar{\tau}_{ij}^{\mathrm{TVE}})$ with increasing variance $V(A/A_0)$ result in an increasing scatter band width. Similar as observed in Section 5.2 for the local effective elastic stiffness components, the probability distributions are asym-

metric with an increasing skewness as the degree of micro structural disorder increases.

A similar investigation is perfomed considering a uniaxial compressive effective strain state with a prescribed macroscopic strain of $\bar{\gamma}_{11} = -0.025$. The results for the probability distributions $F(\bar{\gamma}_{ij}^{\mathrm{TVE}})$ of the local effective strain components $\bar{\gamma}_{11}^{\mathrm{TVE}}$ within the macroscopic loading direction and $\bar{\gamma}_{22}^{\mathrm{TVE}}$ perpendicular to the macroscopic loading direction are presented in Fig. 12(a) and (b), respectively. The probability distributions of the corresponding local effective stress components $\bar{\tau}_{11}^{\mathrm{TVE}}$ and $\bar{\tau}_{22}^{\mathrm{TVE}}$ within and perpendicular to the direction of the applied macroscopic strain are presented in Fig. 12(c) and (d), respectively. Again, three different degrees of micro structural disorder are considered, ranging from a low level of disorder with $V(A/A_0) = 0.5$ up to a high level with $V(A/A_0) = 4.5$.

Compared to the case of uniaxial tension, an increased scatter of the local effective strain components $\bar{\gamma}_{11}^{\mathrm{TVE}}$ and $\bar{\gamma}_{22}^{\mathrm{TVE}}$ is observed. In this context, it should be noticed that positive tensile local effective strains $\bar{\gamma}_{11}^{\mathrm{TVE}}$ and consequently tensile stresses $\bar{\tau}_{11}^{\mathrm{TVE}}$ develop in some of the testing volume elements. Due to strong interactions of neighboring testing volume elements in conjunction with local load redistribution caused by the occurrence of instability effects, a non negligible number of testing volume elements is locally loaded in tensile modes, although the macroscopic applied strain is compressive. The probability of the occurrence of local tensile strain states increases with increasing degree of micro structural disorder (see Fig. 12(a)) whereas only minor effects of the micro structural disorder are observed in all other cases.

Again, non symmetric probability distributions with a non negligible skewness are obtained, especially in case of the local effective strain component $\bar{\gamma}_{11}^{\mathrm{TVE}}$ acting within the macroscoping loading direction (Fig. 12(a)). Hence, the distributions governing the uncertainty in the effective material response of structural foams are essentially non Gaussian so that a complete assessment requires the determination of the probability distributions rather than the consideration of the expectation value and the variance alone.

Two examples for the deformed configurations of micro structures with low and high degrees of micro structural disorder are presented in Fig. 13(a) and (b) in order to highlight the different micro structural mechanisms of deformation. For reasons of a more distinct presentation, an increased level of the applied macroscopic effective strain of $\bar{\gamma}_{11} = -0.1$ is applied. In the deformed configuration, the contemporary presence of ranges with high and low levels of local deformation are clearly visible. Weak local behavior and thus high levels of resulting local deformation are observed especially for large cells in the micro structure with a high degree of disorder in Fig. 13(b). At the same time, a number of Voronoï cells with nearly unchanged shape is observed in the deformed configuration. In general, these cells feature a high local stiffness due to a small size and a small number of cell walls or the cells are surrounded by cells with a similar stiffness.

This result coincides with the experimental and numerical results of other authors (e.g. Papka and Kyriakides, 1994; Silva and Gibson, 1997; Zhu and Mills, 2000) that the effective mechanical behavior of two-dimensional cellular structures in the highly compressed range is strongly governed by localized deformations caused by local micro structural instabilities. Due to the reorientation of the cell walls, this effect might result in several non classical effects such as the development of deformation induced negative (generalized) Poisson's ratios, as they were also observed in a previous numerical study by one of the present authors (Hohe and Becker, 2003). In the present case, the distinct re-orientaion of the cell walls in the vicinity of highly deformed cells is responsible for the possible change in sign of the local deformation compared to the macroscopically applied external deformation observed for some testing volume elements in the compressive load cases. Since the mentioned local deformation effects are equally present for micro structures with both, low and high degrees of micro structural disorder, only minor effects of increasing degrees of disorder are observed in terms of the probability distributions presented in Fig. 12.

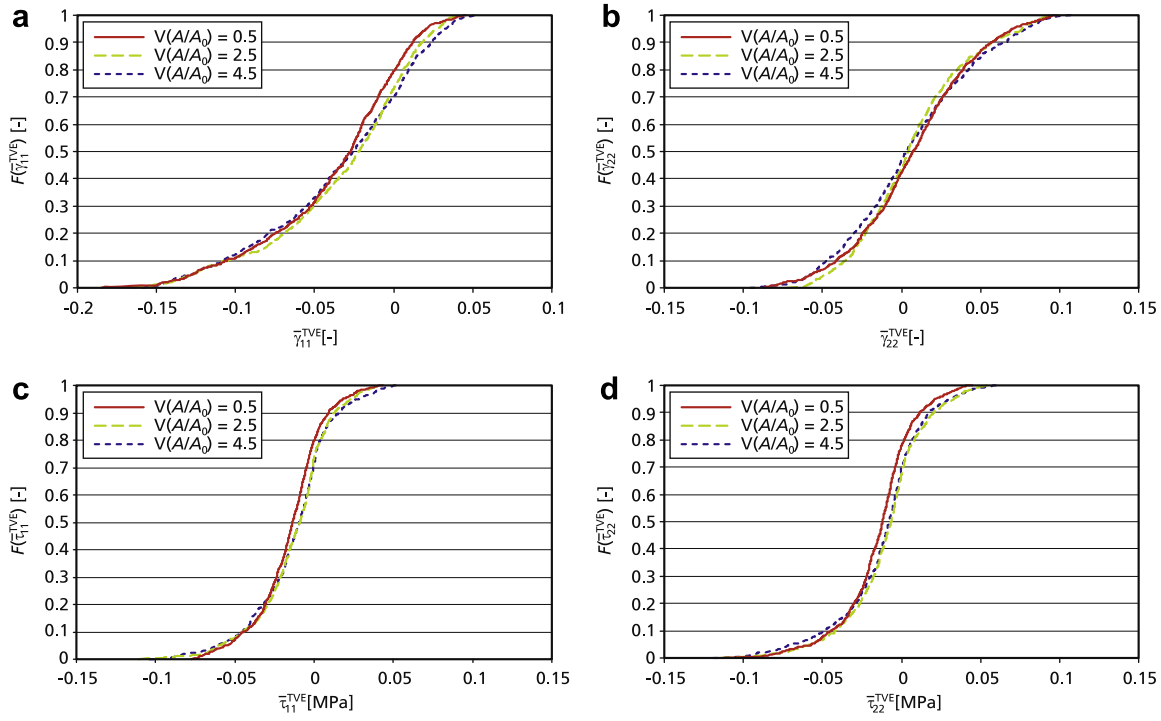

Fig. 12. Effective local strain and stress components in compression, probability distributions: (a) Green-Lagrange normal strain $\bar{\gamma}_{11}$ within the global straining direction, (b) Green Lagrange normal strain $\bar{\gamma}_{22}$ perpendicular to the global straining direction, (c) second Piola-Kirchhoff stress $\bar{\tau}_{11}$ within the global straining direction and (d) second Piola-Kirchhoff stress $\bar{\tau}_{22}$ perpendicular to the global straining direction.

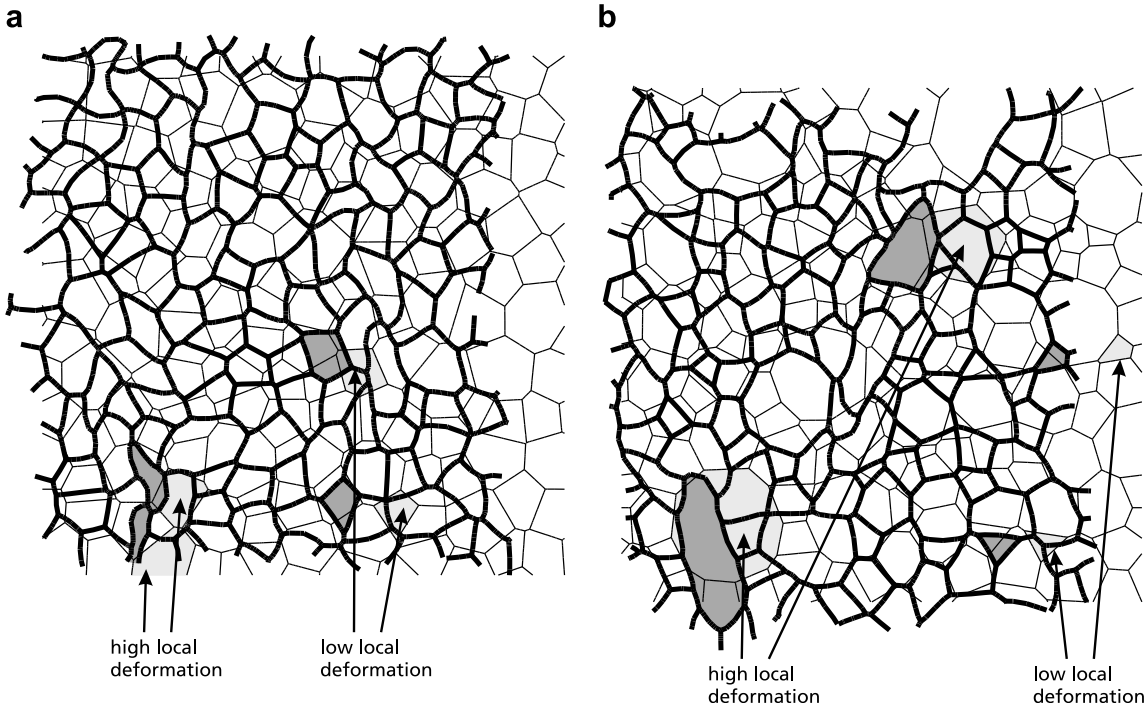

Fig. 13. Deformed configuration with examples of cells with high and low local deformation under effective uniaxial compression with $\bar{\gamma}_{11} = -0.1$: (a) low degree of microstructural disorder and (b) high degree of microstructural disorder.

5.4. Testing volume element size effect

All previous analyses are based on an evaluation directly on the level of the individual testing volume elements according to Fig. 4 forming the lowest meaningful level for a homogenization analysis. On the other hand, larger substructures defined by multiple cell wall intersections and the corresponding cell walls might be used as testing volume elements for the stochastic analysis instead of the smallest possible ones. Due to self-averaging effects, especially the scatter of the results will stongly depend on the size of the underlying testing volume elements.

In order to study the testing volume element size effect in more detail, an analysis based on patches of several neighboring volume elements is performed. In this context, the testing volume element belonging to an individual cell wall intersection is defined as the patch consisting of all previously used minimum size volume elements associated with cell wall intersections featuring an Euclidean distance r to the position of the actual cell wall intersection which is smaller than a prescribed value r_0. The effective properties associated with these patches are determined as the averages of the respective local effective quantities for all cell wall intersections belonging to the patch. The averages of the local effective quantities are determined as the weighted arithmetic averages of the respective quantities where the area of the smallest possible testing volume elements associated with the respective cell wall intersection (see Fig. 4) normalized with the total area of the new testing volume element forms the weight factor.

As an example, the same material as in Section 5.3 is considered, concerning both, the cell wall material as well as the micro structure and its relative density. The computational foam model is generated by means of the Voronoï process in Laguerre geometry using 512 Voronoï cells. The representative volume element is subjected to uniaxial macroscopic states of deformation in the tensile and compressive ranges with $\bar{\gamma}_{11} = 0.025$ and $\bar{\gamma}_{11} = -0.025$, respectively. The resulting probability distributions $F(\bar{\tau}_{ij}^{\mathrm{TVE}})$ for the resulting local effective stress components $\bar{\tau}_{11}^{\mathrm{TVE}}$ and $\bar{\tau}_{22}^{\mathrm{TVE}}$ within and perpendicular to the macroscopic straining direction (x_1-direction) are presented in Fig. 14. In each case, four different radii $\bar{r}_0$, normalized with the edge length of the representative volume element are considered. The corresponding expectation values $E(\bar{\tau}_{ij})$ and variances $V(\bar{\tau}_{ij})$ are presented in Fig. 15. Two different degrees of micro structural disorder are considered. For the low degree of disorder, the cell size distribution features a variance of $V(A/A_0) = 1$ whereas the large degree of disorder is characterized by a cell size distribution with a variance of $V(A/A_0) = 5$.

As it could be expected, a decreasing uncertainty in the local effective stress components $\bar{\tau}_{ij}^{\mathrm{TVE}}$ is obtained with increasing radius $\bar{r}_0$ and thus increasing size of the testing volume elements. Strong effects are observed especially for small radii $\bar{r}_0$, where the variance $V(\bar{\tau}_{ij}^{\mathrm{TVE}})$ features a steep gradient (see Fig. 15). In the same range, the derivatives of the probability distributions $F(\bar{\tau}_{ij}^{\mathrm{TVE}})$ vary rapidly with varying size $\bar{r}_0$ of the testing volume elements. For radii $\bar{r}_0$ larger than $\bar{r}_0 \approx 0.1$, the variances $V(\bar{\tau}_{ij}^{\mathrm{TVE}})$ of the local effective stress components are approaching vanishing values. Consequently, step like probability distributions $F(\bar{\tau}_{ij}^{\mathrm{TVE}})$ are obtained. For testing volume elements of this size, the disorder effects are vanishing, indicating that the size approaches the size necessary for statistically representative volume elements. Nevertheless, even though the variances for $\bar{r}_0 \geqslant 0.1$ are vanishing compared to their initial values in the limit $\bar{r}_0 \to 0$, some scatter in the effective local stress components $\bar{\tau}_{ij}^{\mathrm{TVE}}$ is still present, as it can be observed from the non infinite slopes of the probability distributions shown in Fig. 14. No effect of the testing volume element size $\bar{r}_0$ is obtained in case of the expectation value $E(\bar{\tau}_{ij}^{\mathrm{TVE}})$. Similar effects regarding both, the expectation values and the variances are observed for both, tensile and compressive external loading as well as for both, high and low degrees of micro structural disorder. Differences between the effects to be observed are restricted to the quantitative point of view.

5.5. Correlation

As a final investigation, the correlation of the local effective quantities related to neighboring testing volume elements is

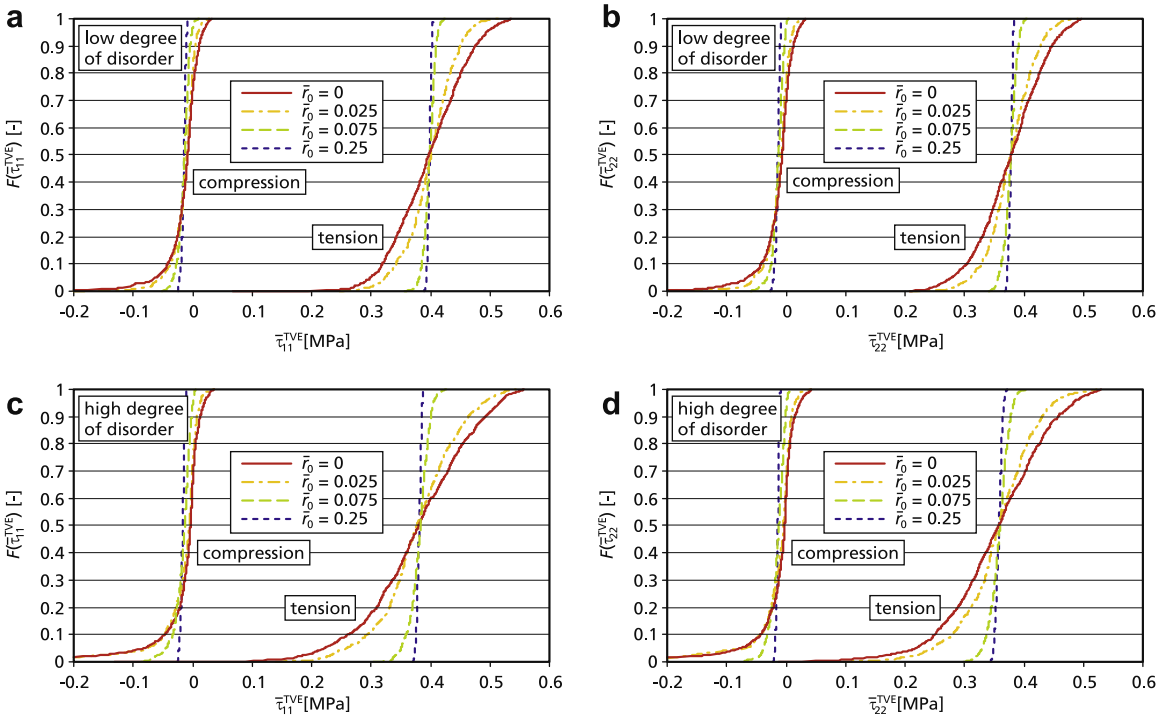

Fig. 14. TVE size effect, probability distributions: (a) and (b) low degrees of disorder, stress within and perpendicular to external straining direction, (c) and (d) high degrees of disorder, stress within and perpendicular to external straining direction.

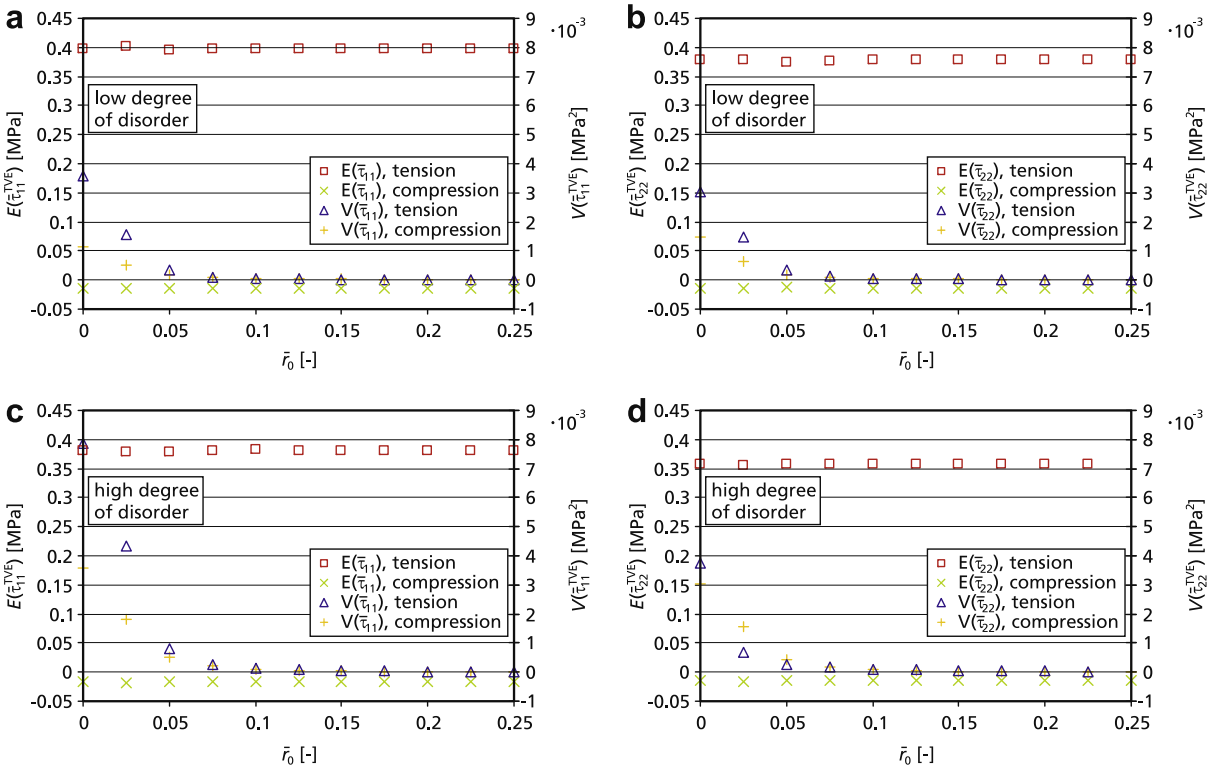

Fig. 15. TVE size effect, expectation values and variances: (a) and (b) low degrees of disorder, stress within and perpendicular to external straining direction, (c) and (d) high degrees of disorder, stress within and perpendicular to external straining direction.

analyzed. As a measure for the spatial variation of a specific local effective quantity Y^{TVE} (local effective stress, strain or stiffness) between testing volume elements no. i and j, the difference

$$\Delta Y^{\mathrm{TVE}(ij)} = |Y^{\mathrm{TVE}(j)} - Y^{\mathrm{TVE}(i)}| \tag{28}$$

is employed. For strong correlations between the local effective properties of neighboring testing volume elements, only small values should be obtained for small Euclidean distances r between the positions of the two testing volume elements whereas arbitrary values $\Delta Y^{\mathrm{TVE}(ij)}$ even for small distances indicate a weak or vanishing correlation.

In order to study the effect of the correlation between the local effective properties of neighboring testing volume elements, the differences $\Delta\bar{\gamma}_{ij}^{\mathrm{TVE}(ij)}$ of the local effective strain components according to Eq. (28) are determined for all possible pairs (i,j) of testing volume elements in the problem considered in Section 5.4. Due to the large number of 512 Voronoï cells (corresponding to a number of 1024 testing volume elements), a huge amount of data is obtained. A restricted subset of this raw data base consisting of every 400th data point is presented in Fig. 16 depending on the distance r normalized with the edge length of the representative volume element. Since an evaluation of possible effects in terms of this presentation is difficult, subsets are considered, consisting of all data obtained for a small distance range defined by $\bar{r} \pm \Delta\bar{r}$. The subsets of the total data base are analyzed in terms of the resulting probability distributions. The results are presented in Fig. 17.

For the tensile macroscopic load case, equal probability distributions for both, the local effective strain components $\bar{\gamma}_{11}^{\mathrm{TVE}}$ within the macroscopic straining direction and the component $\bar{\gamma}_{22}^{\mathrm{TVE}}$ perpendicular to this direction are obtained, whether a low or a high degree of micro structural disorder is considered. This result shows that no distinct effect of the Euclidean distance $\bar{r}$ between two testing volume elements on the relation of their effective mechanical properties is present. In contrast, a correlation effect is observed under compressive external loading. In this case, increasing accumulated probabilities are obtained for small differences $\Delta\bar{\gamma}_{ij}^{\mathrm{TVE}}$, if the distance $\bar{r}$ of the considered testing volume elements decreases. Hence, the local effective strains for testing volume elements with small distances are found to be correlated under compressive macroscopic loading, although the effect is weak. The reason for the presence of a correlation under compression, which is not observed under macroscopic tension is the possible formation of clusters of bands with strain localizations under compression (Silva and Gibson, 1997), which is also observed in Fig. 13 analyzing the deformed configuration under compressive loading conditions.

6. Conclusions

The present study is concerned with a probabilistic homogenization analysis of two-dimensional model foams investigating the effect of micro structural disorder on the effective mechanical properties of the material. In contrast to previous analyses either consisting of a single analysis or a limited number of analyses of a large scale computational foam model or consisting of the repeated execution of analyses of a small scale foam model in a Monte Carlo simulation, a different approach is proposed. This approach consists in a single analysis of a large scale, statistically representative computational foam model. The results of the analysis are evaluated on the base of local testing volume elements as subsets of the entire representative volume element. This approach overcomes the problems of limited stochastic information or limited freedom in the development of the micro structure due to the use of small scale foam models in previous studies. Another advantage is the fact that the analysis of the scatter in the effective material response can be performed on every feasable length scale. This feature is important, since the scatter in the effective material response is strongly related to the considered length scale. Due to self-averaging effects, the scatter decreases with increasing sample sizes.

In most of the analyses performed in the present study, the assessment of the uncertainty of the material is performed on the lowest possible length scale, using testing volume elements consisting of a single cell wall intersection and half of the corresponding adjacent cell walls as the smallest meaningful subsets of the representative volume element for a local homogenization analysis. Nevertheless, the approach can easily be modified towards an assessment of the scatter on larger length scales by recombining adjacent ones of the smallest possible testing volume elements to larger elements. Hence, the probabilistic homogenization procedure proposed in the present study provides a tool for the assessment of the material uncertainties of micro structurally

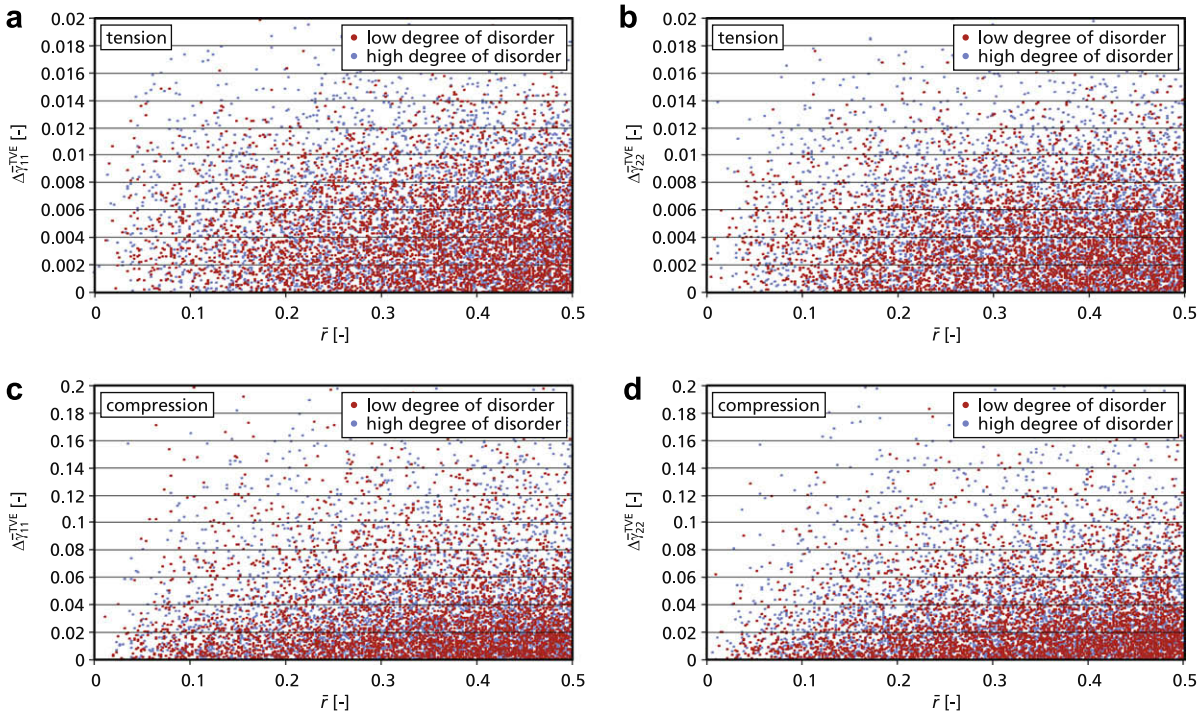

Fig. 16. Correlation, raw data: (a) and (b) tensile external strain, low and high degrees of micro structural disorder, (c) and (d) compressive external strain, low and high degrees of micro structural disorder.

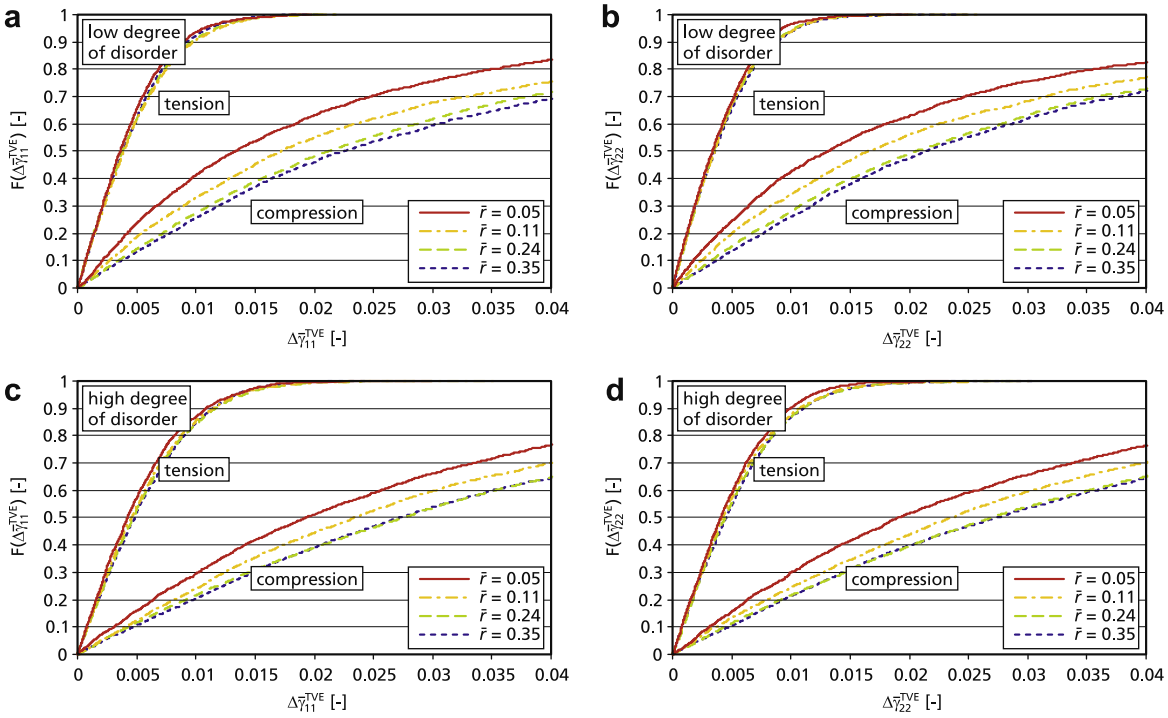

Fig. 17. Testing volume element size effect, probability distributions: (a) and (b) low degrees of disorder, strain within and perpendicular to external straining direction, (c) and (d) high degrees of disorder, strain within and perpendicular to external straining direction.

disordered materials, whether foamed or true multi phase materials, on every desired length scale larger than the smallest meaningful one as governed by the characteristic dimensions of the micro structure. Although only two-dimensional examples are considered in the present contribution, the proposed method can be extended to the three-dimensional case in a straight forward manner.

In an application of the proposed procedure to an uncertainty analysis of structural foams, strong effects of the micro structural disorder on both, the mean effective material response and the corresponding scatter are observed, especially in the finite strain range. Hence, the use of regular periodic foam models in a numerical homogenization analysis of structural foams and other distinctly disordered media might provide inadequate results for the effective material behavior, even if only the mean stress-strain response is considered. The scatter of the effective stresses is found to be governed by both, the scatter in the effective stiffness together with the scatter in the local effective strains. Due to the possible activation of different micro structural modes of deformation, the local effective strains might be subject to a distinct scatter around their expectation value, especially in the compressive range of the effective deformation. The two sets of random variables, the local effective stiffness and the local effective strain components, are highly correlated rather than independent random variables. Hence, an exclusive consideration of the local effective stiffness components might be insufficient.

In the context of an uncertainty analysis of the effective stress and strain components, probability distributions with in some cases strong asymmetric shapes with non negligible skewness are obtained. Hence, the probability density distributions for the mechanical field quantities are essentially non Gaussian. Therefore, a reliable probabilistic homogenization analysis has to be performed directly in terms of the probability distributions of the considered quantities instead of an exclusive assessment in terms of integral parameters as the expectation value and the variance, although these parameters are important means for characterization of the cross relations between the geometric uncertainty of the micro structure and the induced material uncertainty on the macroscopic level of structural hierarchy.

Acknowledgements

This work has in part been supported by the Deutsche Forschungsgemeinschaft (DFG, German research foundation) under Grant No. Ho 1852/6-1. The financial support is gratefully acknowledged.

References

Blazy, J.S., Marie-Louise, A., Forest, S., Chastel, Y., Pineau, A., Awade, A., Grolleron, C., Moussy, F., 2004. Deformation and fracture of aluminium foams under proportional and multi-axial loading: statistical analysis and size effect. International Journal of the Mechanical Sciences 46, 217–244.

Boomsma, K., Poulikakos, D., Zwick, F., 2003. Metal foams as compact high performance heat exchangers. Mechanics of Materials 35, 1161–1176.

Chen, C., Lu, T.J., Fleck, N.A., 1999. Effect of imperfection on the yielding of two-dimensional foams. Journal of the Mechanics and Physics of Solids 47, 2235–2272.

Christensen, R.M., 1987. Sufficient symmetry conditions for isotropy of the elastic moduli tensor. Journal of Applied Mechanics 54, 772–777.

Cuitiño, A.M., Zheng, S., 2003. Taylor averaging on heterogeneous foams. Journal of Composite Materials 37, 701–713.

Daxner, T., Böhm, H.J., Rammerstorfer, F.G., Denzer, R., Maier, M., 2000. Simulation des elasto-plastischen Verhaltens von Metallschaum mit Hilfe von 2D und 3D Einheitszellen-Modellen. Materialwissenschaft und Werkstofftechnik 31, 447–450.

Fan, Z., Wu, Y., Zhao, X., Lu, Y., 2004. Simulation of polychrystalline structure with Voronoï diagram in Laguerre geometry based on random closed packing of spheres. Computational Materials Science 29, 301–308.

Fortes, M.A., Ashby, M.F., 1999. The effect of non-uniformity on the in-plane modulus of honeycombs. Acta Materialia 47, 3469–3473.

Gent, A.N., Thomas, A.G., 1963. Mechanics of foamed elastic materials. Rubber Chemistry and Technology 36, 597–610.

Gibson, L.J., Ashby, M.F., 1982. The mechanics of three-dimensional cellular materials. Proceedings of the Royal Society A 382, 43–59.

Gibson, L.J., Ashby, M.F., 1997. Cellular Solids – Structure and Properties. Cambridge University Press, Cambridge.

Hall, R., 1993. Effective moduli of cellular materials. Journal of Reinforced Plastics and Composites 12, 186–197.

Hohe, J., Becker, W., 2003. Effective mechanical behavior of hyperelastic honeycombs and two-dimensional model foams at finite strain. International Journal of the Mechanical Sciences 45, 891–913.
Hohe, J., Becker, W., 2005. A probabilistic approach to the numerical homogenization of irregular solid foams in the finite strain regime. International Journal of Solids and Structures 42, 3549–3569.
Huyse, L., Maes, M.A., 2001. Random field modeling of elastic properties using homogenization. Journal of Engineering Mechanics 127, 27–36.
Kanit, T., Forest, S., Galliet, I., Mounoury, V., Jeulin, D., 2003. Determination of the size of the representative volume element for random composites: statistical and numerical approach. International Journal of Solids and Structures 40, 3647–3679.
Kim, J.S., Jeong, J.C., Lee, S.J., 2007. Numerical and experimental studies on the deformational behavior of a composite train carbody of the Korean tilting train. Composite Structures 81, 168–175.
Lachihab, A., Sab, K., 2005. Aggregate composites: a contact based modeling. Computational Materials Science 33, 467–490.
Mills, N.J., Fitzgerald, C., Gilchrist, A., Verdejo, R., 2003. Polymer foams for personal protection: cushions, shoes and helmets. Composite Science and Technology 63, 2389–2400.
Mouritz, A.P., Gellert, E., Burchill, P., Challis, K., 2001. Review of advanced composite structures for naval ships and submarines. Composite Structures 53, 21–41.
Ning, H., Janowski, G.M., Vaidya, U.K., Husman, G., 2007. Thermoplastic sandwich structure design and manufacturing for the body panel of mass transit vehicle. Composite Structures 80, 82–91.
Ostoja-Starzewski, M., 2006. Material spatial randomness: from statistical to representative volume element. Probabilistic Engineering Mechanics 21, 112–132.
Papka, S.C., Kyriakides, S., 1994. In-plane compressive response and crushing of honeycomb. Journal of the Mechanics and Physics of Solids 42, 1499–1532.
Patel, M.R., Finnie, I., 1970. Structural features and mechanical properties of rigid cellular plastics. Journal of Materials 5, 909–932.
Ramamurty, U., Paul, A., 2004. Variability in mechanical properties of a metal foam. Acta Materialia 52, 869–876.
Roberts, A.P., Garboczi, E.J., 2002. Elastic properties of model random three-dimensional open-cell solids. Journal of the Mechanics and Physics of Solids 50, 33–55.
Shulmeister, V., van der Burg, M.W.D., van der Giessen, E., Marissen, R., 1998. A numerical study of large deformation of low-density elastomeric open-cell foams. Mechanics of Materials 30, 125–140.
Silva, M.J., Gibson, L.J., 1997. The effects of non-periodic microstructure and defects on the compressive strength of two-dimensional cellular solids. International Journal of the Mechanical Sciences 39, 549–563.
Thomson (Lord Kelvin), W., 1887. On the division of space with minimum partitional area. Philosophical Magazine 24, 503–514.
Torquato, S., 2002. Random Heterogeneous Materials – Microstructure and Macroscopic Properties. Springer Science & Business Media, New York.
Voronoï, G., 1908. Nouvelles applications des paramètres continus à la théorie des formes quadratiques. Journal für Reine und Angewandte Mathematik 134, 198–312.
Warren, W.E., Kraynik, A.M., 1988. The linear elastic properties of open-cell foams. Journal of Applied Mechanics 55, 341–346.
Warren, W.E., Kraynik, A.M., 1997. Linear elastic behavior of a low-density Kelvin foam with open cells. Journal of Applied Mechanics 64, 787–794.
Weaire, D., Phelan, R., 1994. A counter-example to Kelvin's conjecture on minimal surfaces. Philosophical Magazine Letters 69, 107–110.
Zhu, H.X., Hobdell, J.R., Windle, A.H., 2000. Effects of cell irregularity on the elastic properties of open-cell foams. Acta Materialia 48, 4893–4900.
Zhu, H.X., Mills, N.J., 2000. The in-plane non-linear compression of regular honeycombs. International Journal of Solids and Structures 37, 1931–1949.